Article

SOURCE DATA | TRANSPARENT PROCESS

THE EMBO JOURNAL

TFAM loss induces nuclear actin assembly upon mDia2 malonylation to promote liver cancer metastasis

Qichao Huang[1,*,†], Dan Wu[1,†], Jing Zhao[1,†], Zeyu Yan[2], Lin Chen[1], Shanshan Guo[1], Dalin Wang[3], Chong Yuan[1], Yinping Wang[1], Xiaoli Liu[1] & Jinliang Xing[1,**]

Abstract

The mechanisms underlying cancer metastasis remain poorly understood. Here, we report that TFAM deficiency rapidly and stably induced spontaneous lung metastasis in mice with liver cancer. Interestingly, unexpected polymerization of nuclear actin was observed in TFAM-knockdown HCC cells when cytoskeleton was examined. Polymerization of nuclear actin is causally linked to the high-metastatic ability of HCC cells by modulating chromatin accessibility and coordinating the expression of genes associated with extracellular matrix remodeling, angiogenesis, and cell migration. Mechanistically, TFAM deficiency blocked the TCA cycle and increased the intracellular malonyl-CoA levels. Malonylation of mDia2, which drives actin assembly, promotes its nuclear translocation. Importantly, inhibition of malonyl-CoA production or nuclear actin polymerization significantly impeded the spread of HCC cells in mice. Moreover, TFAM was significantly downregulated in metastatic HCC tissues and was associated with overall survival and time to tumor recurrence of HCC patients. Taken together, our study connects mitochondria to the metastasis of human cancer via uncovered mitochondria-to-nucleus retrograde signaling, indicating that TFAM may serve as an effective target to block HCC metastasis.

Keywords HCC; metastasis; mitochondrial transcription factor A; nuclear F-actin
Subject Categories Cancer; Cell Adhesion, Polarity & Cytoskeleton; Metabolism
DOI 10.15252/embj.2021110324 | Received 8 December 2021 | Revised 30 March 2022 | Accepted 1 April 2022
The EMBO Journal (2022) e110324

Introduction

Hepatocellular carcinoma (HCC) is the second leading cause of cancer-related death in humans worldwide. The most common reasons for HCC treatment failure are metastasis and recurrence (Llovet *et al*, 2021). Therefore, uncovering the mechanisms responsible for metastasis may reveal unappreciated vulnerabilities of cancer cells. Previous studies have shown that several key biological processes such as cell migration, extracellular matrix remodeling, and angiogenesis are often activated and play essential roles in metastasis. However, the cellular and molecular mechanisms responsible for activation of these processes are not completely understood.

The cytoplasmic actin cytoskeleton is a dynamic network composed of actin polymers (also known as actin filaments or F-actin). The reorganization of the F-actin structure at the leading edge has been well studied for its role in the invasive and metastatic phenotypes of cancer cells. In contrast, the presence of actin within the nucleus has long been recognized, but its dynamic assembly into filamentous structures is under debate for decades (Percipalle & Vartiainen, 2019). Recently, improved microscopy techniques and the development of actin probes have allowed the direct visualization of nuclear dynamic actin assembly. Since then, dynamic actin polymerization in the nucleus of living cells has been described in response to several stimuli, including serum stimulation, DNA damage, and viral infection, which has been systematically summarized by Svenja Ulferts (Ulferts *et al*, 2021). Notably, recent studies have also indicated that actin accumulates in the nuclei of tumor cells, although a classical nuclear localization sequence (NLS) was not found. In contrast, many actin-binding proteins, such as the formin family (including mDia2), profilin, and cofilin, contain NLS and regulate actin nuclear transportation, polymerization, and depolymerization (Kristó *et al*, 2016). For example, nuclear actin filament assembly was observed during cell spreading and appeared to be mediated by mDia formins, which are the major actin-binding proteins. However, the exact role of polymerized actin in the nucleus during cancer cell metastasis remains unknown.

Mitochondria are intracellular organelles that produce most of the energy, metabolites, and reactive oxygen species. These functions also determine the crucial role of mitochondria in cancer

1 State Key Laboratory of Cancer Biology and Department of Physiology and Pathophysiology, Fourth Military Medical University, Xi'an, China
2 Department of General Surgery, Tangdu Hospital, Fourth Military Medical University, Xi'an, China
3 Department of Hepatobiliary Surgery, Xijing Hospital, Fourth Military Medical University, Xi'an, China
*Corresponding author. Tel: +8602984774551; E-mail: huangqichao1@163.com
**Corresponding author. Tel: +8602984774551; E-mail: xingjinliang@163.com
†These authors contributed equally to this work

progression, including metastasis. Recently, several studies have established an association between mitochondrial metabolic alterations and tumor metastasis via mitochondria-to-nucleus retrograde signaling (Gao *et al*, 2007; Zhou *et al*, 2009). Actually, it is rapidly appreciated that metabolites in the mitochondrial tricarboxylic acid (TCA) cycle are involved in controlling post-translational modifications of proteins, chromatin modifications, and DNA methylation (Martínez-Reyes & Chandel, 2020). For instance, the most prominent signaling function of acetyl-CoA is related to its ability to provide acetyl groups for acetylation, one of the major post-translational protein modifications involved in tumor metastasis (Lu *et al*, 2019). Similarly, malonyl-CoA-mediated malonylation is a recently identified, evolutionarily conserved modification that is predicted to change its charge and affect interactions between proteins (Peng *et al*, 2011). However, much work remains to be done to understand how these metabolites affect the core steps of metastasis.

Mitochondrial transcription factor A (TFAM) plays a pivotal role in the regulation of mitochondrial biogenesis and the TCA cycle. Recently, we found that TFAM is overexpressed in colitis-associated cancer (CAC) tissues and exerts a tumor-promoting role by enhancing mitochondrial oxidative phosphorylation in CAC progression. Moreover, TFAM has also been implicated in malignant behavior by shaping invasion gene signatures in melanoma cells (Araujo *et al*, 2018). Here, we report that TFAM loss induces spontaneous lung metastasis in mouse liver cancer models driven by hydrodynamic injection of oncogenes or DEN treatment. We further identified a critical role of TFAM in the polymerization of nuclear actin and HCC metastasis. Our study reveals the potential value of TFAM as a prognostic marker and therapeutic target for combating HCC metastasis.

Results

TFAM knockout induced spontaneous lung metastasis in mouse liver cancer models

To evaluate the effects of abnormal mitochondrial metabolic function and morphology on the metastasis of liver cancer, we generated liver-specific TFAM, MFN1, and MFN2 knockout mouse models (Appendix Fig S1A and B), which showed no signs of tumorigenesis over a 20 weeks period (Appendix Fig S1C). Then, well-characterized mouse liver tumorigenesis was induced by the hydrodynamic co-expression of the oncogenes Akt and β-catenin. Our results demonstrated that only TFAM knockout induced spontaneous lung metastasis in Akt/β-catenin-driven HCC (Fig 1A), although all three knockouts increased tumor burden (Figs 1D and EV1A and B). Moreover, heterozygous knockout of TFAM ($TFAM^{+/LKO}$) caused a moderate decrease in TFAM expression (Appendix Fig S1B) and a lower rate of lung metastasis compared to the homozygous knockout of TFAM (43.2% versus 68.8%, $P < 0.001$, Fig 1A). In addition, the average number of micrometastases in $TFAM^{+/LKO}$ mice was lower than that in $TFAM^{LKO}$ mice (3.2 ± 1.9 versus 15.8 ± 6.9, $P < 0.001$), suggesting a dose-dependent effect of TFAM deficiency on metastasis (Fig 1A). However, no significant difference of tumor burden was observed between $TFAM^{+/LKO}$ and $TFAM^{LKO}$ mice (Fig 1D). Importantly, the dose-dependent effect of TFAM knockout on lung metastases was successfully reproduced in other mouse liver cancer models, either by Akt/N-ras injection (Figs 1B and EV1C and D) or by diethylnitrosamine (DEN) plus CCl_4 treatment, a widely used chemical induction (Figs 1C and EV1E). Interestingly, although the tumor burden was relatively small in DEN-induced HCC (Fig EV1G), lung metastasis still occurred in $TFAM^{+/LKO}$ and $TFAM^{LKO}$ mice (Fig 1C), implying that there might be no direct correlation between tumor burden and HCC metastasis mediated by TFAM deficiency. Therefore, to further exclude the possibility that the relatively small tumor burden in control mice ($TFAM^{+/f}$ and $TFAM^{f/f}$) was the main reason for the lack of lung metastasis, the observation time for control mice with oncogene injection was prolonged. Again, no lung metastasis was found (Fig 1D) when the tumor burden in control mice (Figs 1D and EV1C and D. 18 weeks for Akt/β-catenin group or 14 weeks for Akt/N-ras group) was comparable to that of $TFAM^{LKO}$ or $TFAM^{+/LKO}$ mice with multiple lung metastases (12 weeks for Akt/β-catenin group or 10 weeks for Akt/N-ras group).

Downregulated TFAM significantly contributes to the metastasis of HCC cells *in vitro and in vivo*

Next, TFAM expression was analyzed in a panel of human HCC cell lines with different metastatic potentials. We found that the expression of TFAM was significantly downregulated in HCC cell lines compared with normal hepatocyte LO2 cells and non-tumor liver tissues. Furthermore, HCC cell lines with high metastatic ability, including MHCC-97H, HLE, and LM3, had much lower expression of TFAM than those with low metastatic ability, such as SNU-368 and SNU-739 (Fig 2A and B). Next, both *in vitro* and *in vivo* gain- and loss-of-function studies were performed to evaluate the effect of TFAM on the metastatic ability of human HCC cells. As shown in Fig 2C–E and Appendix Fig S2A–C, TFAM knockdown significantly enhanced the migration and invasion abilities of HCC cells. In contrast, TFAM overexpression dramatically inhibited the migration and invasion abilities of HCC cells. Bioluminescence imaging analyses revealed that TFAM knockdown significantly promoted the spread of HCC cells in mice, whereas overexpression of TFAM exerted the opposite effect (Fig 2F). Lung metastasis was then evaluated by H&E staining. As shown in Fig 2G–I, the TFAM-knockdown group had a much higher number of lung metastatic

Figure 1. TFAM knockout induced spontaneous lung metastasis in mouse liver cancer models.

A Gross images and H&E staining of lungs from liver-specific gene knockout mice with hydrodynamic tail vein injection of Akt and β-catenin. Scheme of the experiment was shown. Scale bars, 1 mm.

B, C Gross images and H&E staining of lungs from $TFAM^{+/LKO}$ or $TFAM^{LKO}$ mice injected with Akt/N-ras or treatment with DEN and CCl_4. Scale bars, 1 mm.

D Gross images and H&E staining of lung and liver from $TFAM^{+/LKO}$ or $TFAM^{LKO}$ mice injected with Akt/β-catenin. Different time points were shown. Liver/body weight ratio and percentage of microscopic tumor area was used as the measurements of the tumor burden. Scale bars, 1 mm (lung); 50 μm (liver).

Data information: Sample sizes of about 30 mice per group is shown when calculating the metastasis rate or tumor burden.

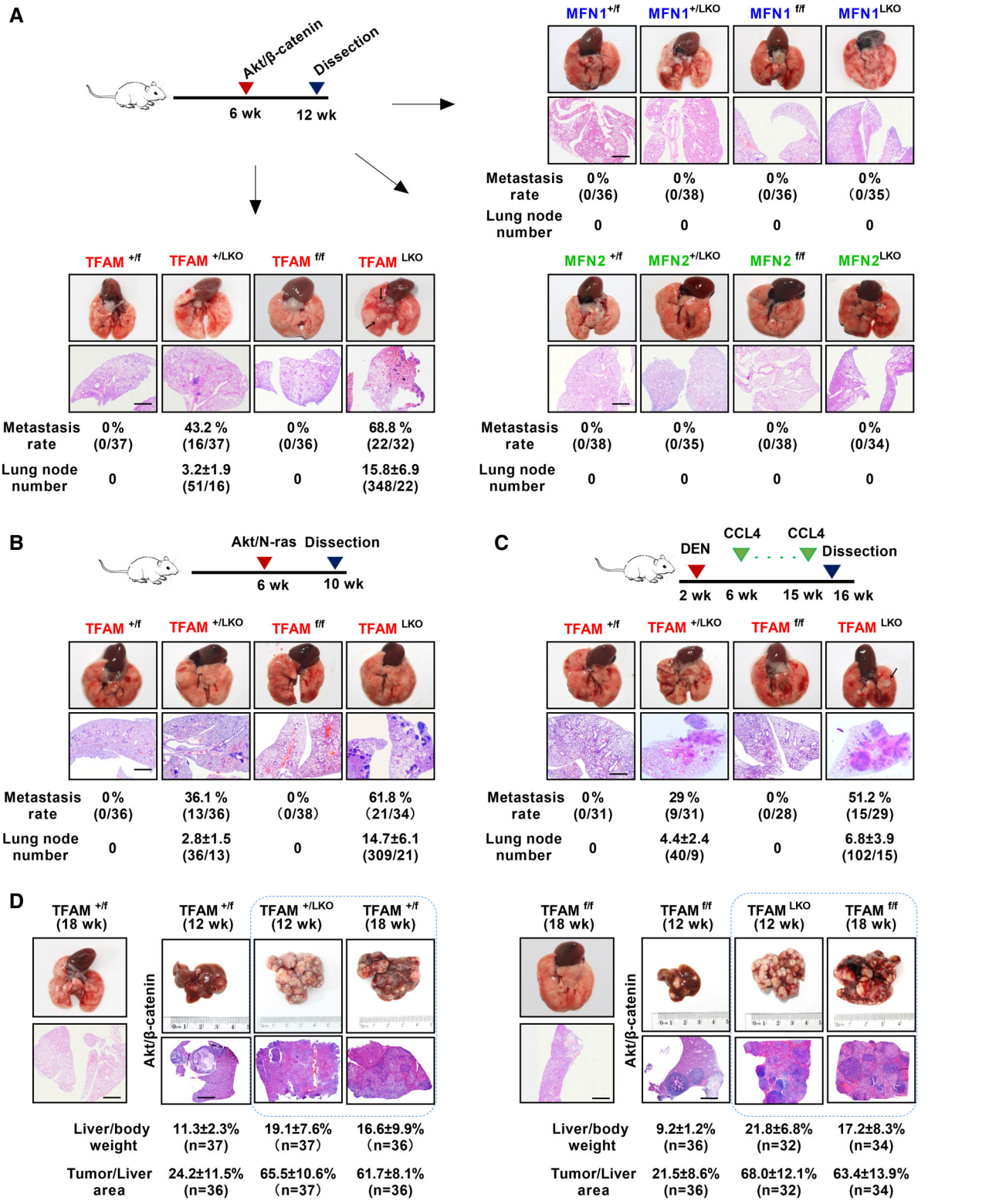

Figure 1.

lesions and a higher incidence of lung metastasis than the control group. In contrast, a lower incidence of metastasis and lesions was found in nude mice bearing orthotopic xenografts of HCC cells overexpressing TFAM. Moreover, TFAM knockdown in HCC cells remarkably shortened the lifespan of mice, whereas TFAM overexpression prolonged the lifespan (Fig 2J).

Downregulated TFAM induced polymerization of nuclear actin in HCC cells

Actin filament (F-actin, polymers of globular actin) remodeling, which facilitates pseudopodia formation and focal adhesion turnover, is a basic mechanism that is critical for cancer metastasis (Venit *et al*, 2020). In this study, phalloidin, a high-affinity F-actin probe, was used. Surprisingly, unexpected polymerization of nuclear actin was observed in the TFAM-knockdown cells. Compared to the control or MFN2 knockdown cells, HCC cells with TFAM knockdown showed much stronger nuclear F-actin staining (Figs 3A and D, and EV2A and B). The 3D reconstruction of z-stacks with IMARIS software strongly supported the nuclear location of thick F-actin. In contrast, TFAM overexpression significantly decreased the nuclear F-actin staining intensity in HCC cells (Figs 3A and D, and EV2A, Movie EV1)). LifeAct, a short F-actin-binding

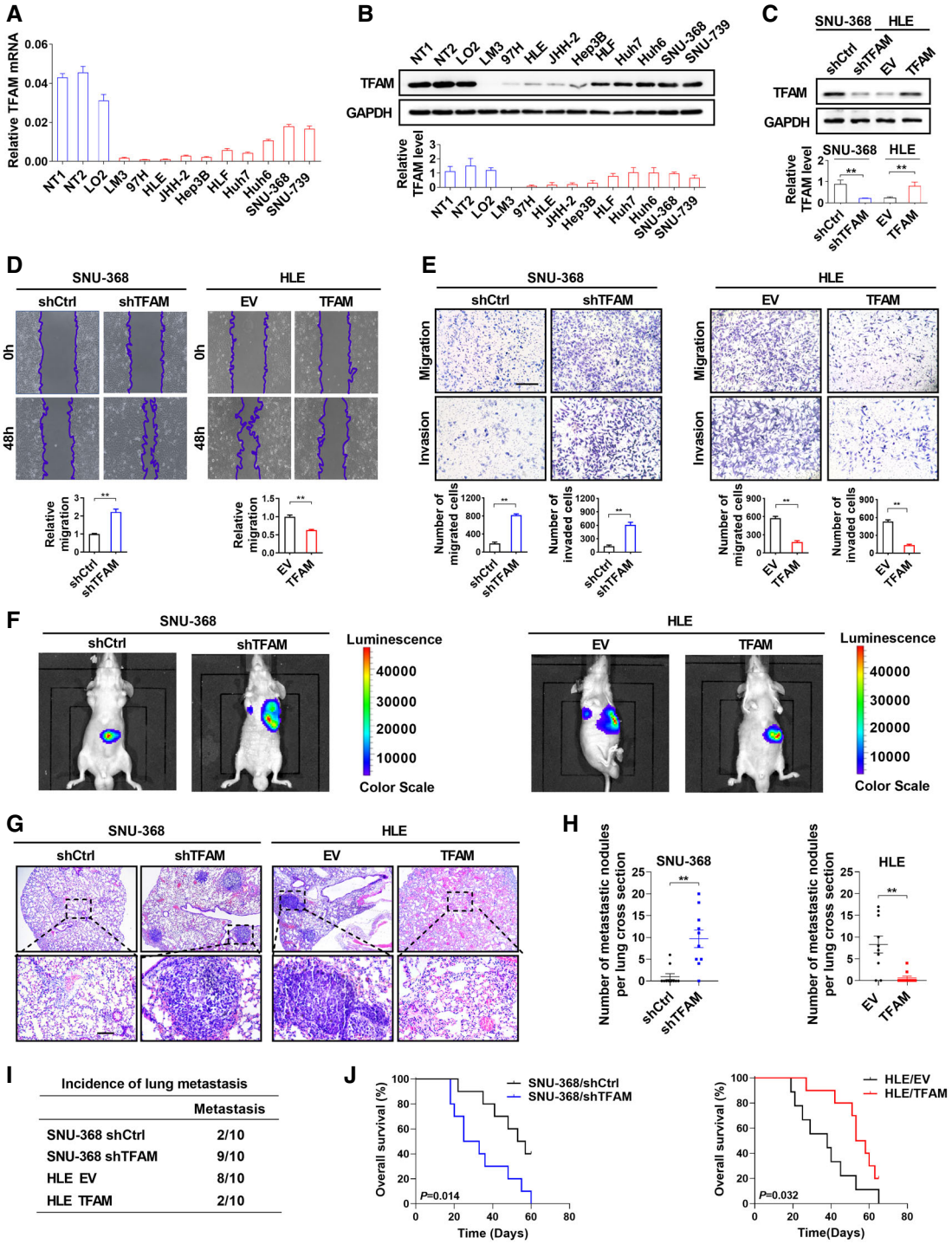

Figure 2.

Figure 2. Downregulated TFAM significantly contributes to the metastasis of HCC cells *in vitro* and *in vivo*.

A, B qRT–PCR and Western blot assays for the expression level of TFAM in ten HCC cell lines, one normal liver cell line (LO2) and two non-tumor liver tissues. The protein level was quantified as ratios between TFAM and GAPDH ($n = 3$ independent experiments).

C Western blot and quantitative analysis for the expression of TFAM in HCC cells with TFAM stable knockdown and control cells ($n = 3$ independent experiments). shCtrl, control shRNA; shTFAM, shRNA against TFAM; EV, empty vector; TFAM, expression vector encoding TFAM.

D, E Wound-healing migration assay (D) and Transwell migration and invasion assays (E) for HCC cells with treatment as indicated ($n = 3$ independent experiments). Scale bars, 100 μm.

F SNU-368 cells with TFAM knockdown or HLE cells with TFAM overexpression were infected with firefly luciferase-expressing lentivirus and transplanted into livers of nude mice. Representative bioluminescent imaging for each group ($n = 10$) is shown.

G Representative H&E images of lung metastasis in mice used in (F). Scale bars, 100 μm.

H, I Number of metastatic nodules per lung (H) and the incidence of lung metastasis (I) in mice used in (F).

J Kaplan–Meier survival curves for mice inoculated with orthotopic HCC cells as indicated. $n = 10$ per group.

Data information: Graphs show mean ± SEM, two-tailed unpaired *t*-test. $^{**}P < 0.01$.
Source data are available online for this figure.

peptide, was also used in living HCC cells, and very similar results were obtained (Figs 3B and EV2C, Movie EV2). To confirm these findings, human HCC tissues were analyzed in the presence of phalloidin. Our results showed that the distribution of F-actin was disturbed in the HCC cells (Fig 3C and Movie EV3). Importantly, the level of nuclear F-actin was significantly higher in HCC cells with low TFAM expression than in those with high TFAM expression (Fig 3D). These findings indicate that TFAM knockdown induces the polymerization of nuclear actin in HCC cells.

Nuclear actin polymerization is necessary for downregulated TFAM-induced metastasis of HCC cells

To address whether nuclear actin polymerization is causally linked to the high metastatic ability of HCC cells, we used non-polymerizable R62D mutant actin with the NLS peptide. Quantitative PCR (qPCR) analysis showed no significant difference between the expression levels of R62D and WT actin in HCC cells (Fig EV2D). Additionally, their nuclear localization was verified by fusion proteins containing GFP (Appendix Fig S3). As shown in Fig 4A, the expression of mutant actin induced the depolymerization of nuclear actin in SNU-368 cells with TFAM knockdown or in HLE cells with a low TFAM expression background and strongly reversed TFAM knockdown-induced migration and invasion of HCC cells (Figs 4B and C, and EV2E and F). Bioluminescence imaging analyses revealed that the expression of R62D mutant actin significantly inhibited the spread of HCC cells in mice compared to that in the WT actin group (Fig 4D). Lung metastasis was further evaluated by H&E staining. As shown in Fig 4E–G, the R62D mutant actin group had a much lower number of lung metastatic lesions and incidence of lung metastasis. Moreover, the expression of R62D mutant actin in HCC cells remarkably shortened the lifespan of mice, whereas TFAM overexpression prolonged the lifespan (Fig 4H).

Downregulated TFAM induced the expression of metastatic genes in a nuclear F-actin-dependent way

Recent studies have shown that nuclear F-actin interacts with chromosomes and plays an important role in chromosome dynamics and gene transcription (Baarlink *et al*, 2013; Spichal *et al*, 2016; Caridi *et al*, 2018; Schrank *et al*, 2018). Therefore, we investigated chromatin accessibility in HCC cells with TFAM knockdown using ATAC-seq. Moreover, the differentially expressed genes (DEGs) between HCC cells with TFAM knockdown and control cells were identified by RNA sequencing. We then integrated the ATAC-seq data with the DEGs to obtain genes (ATAC-DEGs; Dataset EV1) that were directly regulated by TFAM knockdown at the transcriptional level. In total, 1,232 ATAC-DEGs were identified, of which 747 (60.63%) were upregulated and 485 (39.37%) were downregulated, showing an obvious increase in overall accessibility (Fig 5A). Moreover, ingenuity pathway analysis for ATAC-DEGs demonstrated metastasis-related GO terms were consistently deregulated, including extracellular matrix (ECM) remodeling, angiogenesis, cell migration, and adhesion (Fig 5B). ECM remodeling and angiogenesis were further confirmed in TFAM-modeled HCC cells (Appendix Fig S4A and B). KEGG pathways involved in metastasis and tumorigenesis were also enriched, including the MAPK, PI3K-Akt, Hif-1, FoxO, and ECM-receptor interaction signaling pathways (Fig 5C). Moreover, Fig 5D shows the chromatin accessibility around fibronectin 1 (FN1), IL-6, integrinβ3 (ITGB3), and TGFβ genes, which are key players in metastasis and are listed in the top 10 ATAC-DEGs. The upregulated expression of these genes was confirmed by qPCR, Western blotting, and ELISA in human HCC cells and mouse liver cancer tissues (Fig 5E–G and Appendix Fig S4C). Moreover, our results demonstrated that the expression of the non-polymerizable R62D mutant β-actin significantly decreased the expression of FN1, IL-6, TGFβ, and ITGB3 in HCC cells (Fig 5H and I).

Downregulated TFAM induced nuclear translocation of mDia2 to promote nuclear actin polymerization

To gain further mechanistic insights into downregulated TFAM-induced nuclear actin polymerization, we compared the levels of actin in whole cell lysates, nuclear and cytoplasmic fractions between cells with TFAM-knockdown and control cells and found no significant differences between the two groups (Fig EV3A and B). Several key actin-binding proteins (ABPs) were then identified. We noted that the protein levels of three ABPs, mDia2, cofilin, and profilin, were affected by TFAM in the nuclear fraction of HCC cells, among which mDia2 presented the greatest expression alteration (Figs 6A and EV3C). We further verified these results in mouse liver tumor tissues induced by Akt/β-catenin and found that mDia2 was still markedly increased in the nuclear fraction of tumors developed from $TFAM^{LKO}$ mice (Figs 6B and EV3D). Notably, fluorescence microscopy analysis demonstrated that TFAM knockdown promoted the nuclear translocation of mDia2-GFP (or endogenous mDia2) in

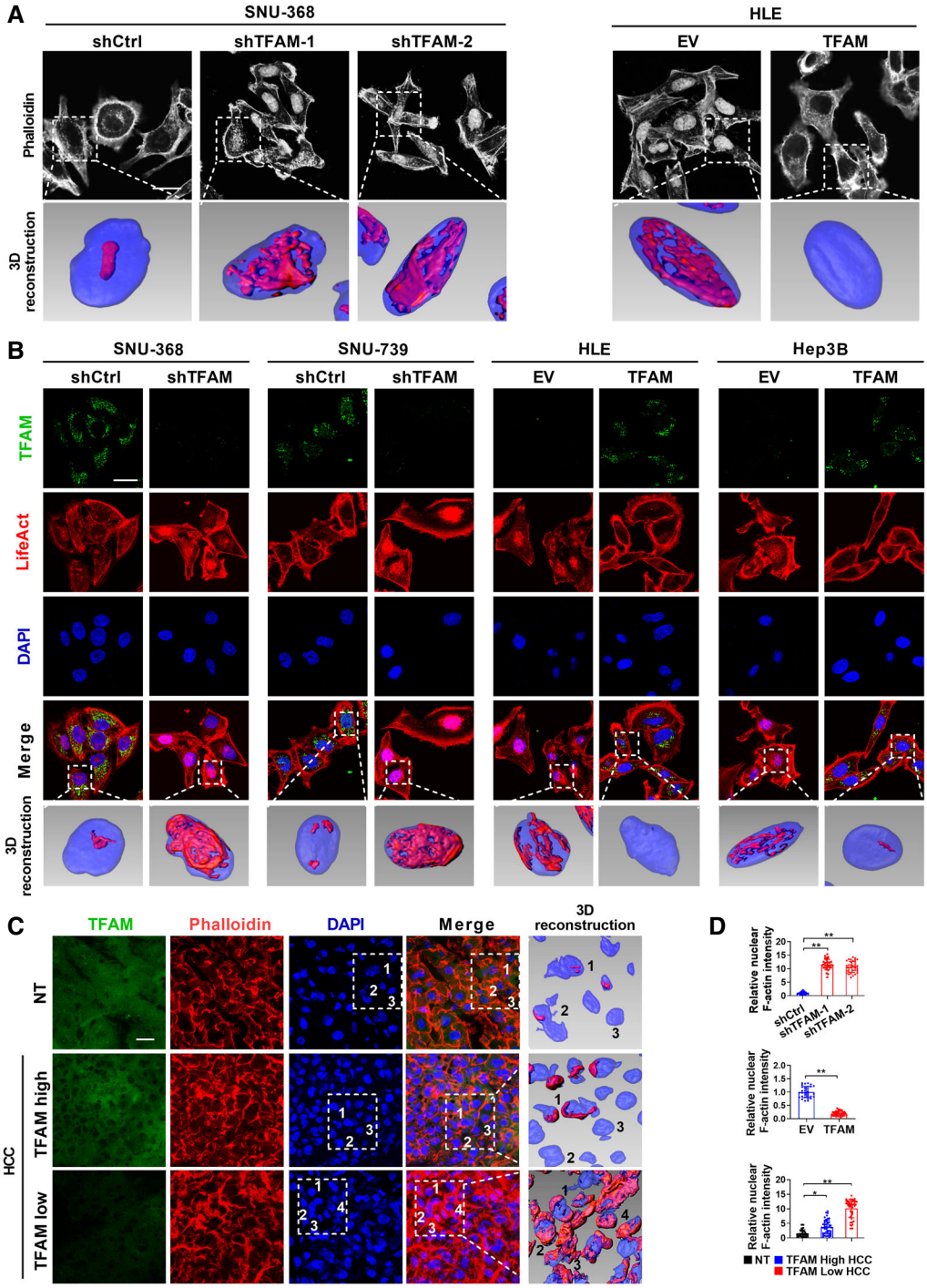

Figure 3. Downregulated TFAM induced polymerization of nuclear actin in HCC cells.

A, B Representative confocal microscopy images of F-actin and 3D reconstruction of z-stacks from nuclear region with IMARIS software in Phalloidin-stained HCC cells (A) and LifeAct-mCherry Venus expressing cells with treatment as indicated (B) (n = 3 independent experiments). Red: Phalloidin or LifeAct, Blue: DAPI. shCtrl, control shRNA; shTFAM, shRNA against TFAM; EV, empty vector; TFAM, expression vector encoding TFAM. Scale bars, 20 μm for microscopy images, 40 μm for 3D reconstruction.

C Immunofluorescence analysis of TFAM and Phalloidin staining in human HCC cells from paired clinical samples (n = 100). The 3D reconstruction of z-stacks from nuclear region is showed in the right side. Red: LifeAct, Blue: DAPI, Green: TFAM. Scale bars, 20 μm for microscopy images, 40 μm for 3D reconstruction.

D Statistical analysis for fluorescent intensity of nuclear F-actin in (A), (B), and (C). Fluorescence intensity are quantified from at least 30 cells for each group in (A) and (B). One-way ANOVA. *P < 0.05; **P < 0.01.

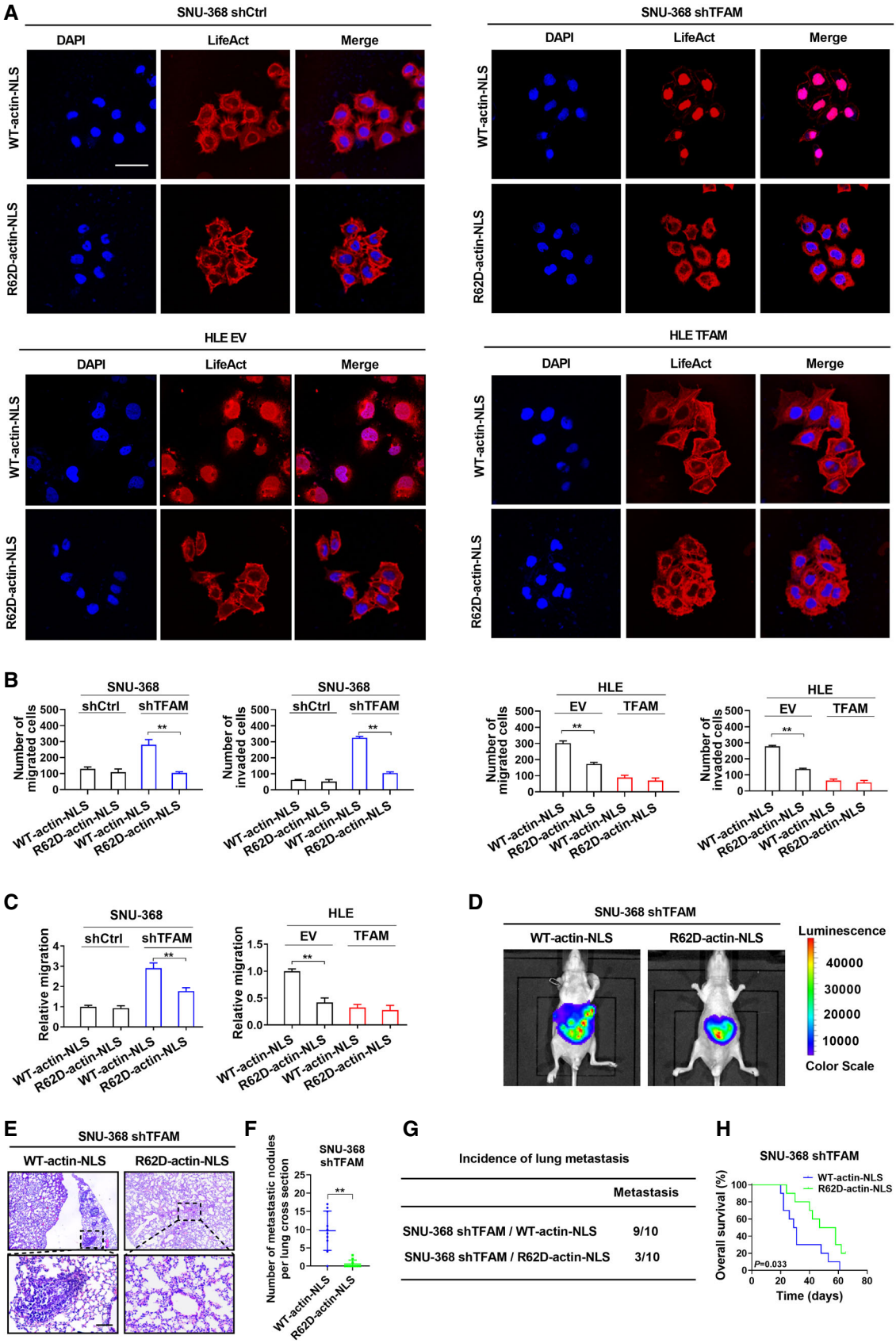
A
SNU-368 shCtrl
SNU-368 shTFAM
HLE EV
HLE TFAM
DAPI
LifeAct
Merge
WT-actin-NLS
R62D-actin-NLS
B
SNU-368
HLE
shCtrl
shTFAM
EV
TFAM
Number of migrated cells
Number of invaded cells
C
Relative migration
D
SNU-368 shTFAM
Luminescence
40000
30000
20000
10000
Color Scale
E
F
Number of metastastic nodules per lung cross section
G
Incidence of lung metastasis
Metastasis
SNU-368 shTFAM / WT-actin-NLS 9/10
SNU-368 shTFAM / R62D-actin-NLS 3/10
H
Overall survival (%)
Time (days)
P=0.033

Figure 4.

Figure 4. Nuclear actin polymerization is necessary for downregulated TFAM-induced metastasis of HCC cells.

A Representative images of F-actin in Lifeact-mCherry Venus expressing cells with treatment as indicated (n = 3 independent experiments). WT-actin-NLS, expression vector encoding NLS-tagged wild-type actin (WT); R62D-actin-NLS, expression vector encoding NLS-tagged non-polymerizable actin mutant (R62D). Scale bars, 20 μm.

B, C Transwell and wound-healing migration analysis for HCC cells with treatment as indicated (n = 3 independent experiments).

D SNU-368 shTFAM cells with R62D-actin-NLS or WT-actin-NLS were infected with firefly luciferase-expressing lentivirus and transplanted into livers of nude mice. Representative bioluminescent imaging for each group (n = 10)

E Representative H&E images of lung metastasis in mice used in (D). Scale bars, 100 μm.

F, G Number of metastatic nodules per lung in mice used in (F) and the incidence of lung metastasis (G) in mice used in (D).

H Kaplan–Meier survival curves for mice inoculated with orthotopic HCC cells as indicated. n = 10 per group.

Data information: Graphs show mean ± SEM, two-tailed unpaired t-test. $^{**}P < 0.01$.

both SNU-368 and SNU-739 cells (Figs 6C and EV3E and F). To further illustrate the direct role of mDia2 in TFAM-related nuclear actin polymerization, we knocked down mDia2 in SNU-368 shTFAM cells and found that nuclear F-actin was depolymerized compared to control cells. Moreover, the re-expression of full-length mDia2 in mDia2 knockdown HCC cells, but not the truncated mDia2 with NLS deletion, significantly reversed this effect (Figs 6D and EV3G).

As expected, knockdown of mDia2 inhibited the migration and invasion of SNU-368 cells induced by TFAM knockdown, implying that mDia2-mediated nuclear actin polymerization is involved in this process (Fig EV3H). The clinical relevance of mDia2 nuclear translocation was analyzed in human HCC tissues. Our results demonstrated that the levels of nuclear mDia2 were significantly higher in metastatic HCC tissues than in paired non-tumor liver tissues or non-metastatic HCC tissues (Fig 6E and F). This result was further confirmed in $TFAM^{LKO}$ mice, where the level of nuclear mDia2 in lung metastasis tissues was much higher than that in primary liver tumor tissues (Fig 6G). Moreover, the positive rate of nuclear mDia2 staining in human HCC was negatively associated with the expression level of TFAM and positively associated with the level of nuclear F-actin (Figs 6H and I, and EV3I).

Downregulated TFAM induced malonylation of mDia2 to promote its nuclear translocation

Post-translational modifications (PTMs) have important effects on subcellular protein localization. Recent studies have revealed that a large number of metabolites can form PTMs (Figlia *et al*, 2020). Therefore, we evaluated several key metabolites in glucose metabolism by targeted metabolomics and found that the levels of acetyl-CoA, oxaloacetic, and malate were decreased in the mitochondria of HCC cells with TFAM-knockdown, whereas citrate levels were increased in the mitochondria, implying blockage of the tricarboxylic acid cycle. In contrast, the levels of citrate and acetyl-CoA were increased in the cytoplasm of HCC cells with TFAM knockdown, which further indicated an increased citrate-malate shuttle (Figs 7A and EV4A and Dataset EV2). Moreover, the elevation of acetyl-CoA and its derivative, malonyl-CoA, was confirmed by ELISA (Fig 7B). Citrate has been shown to directly regulates acetyl-CoA carboxylase (ACC) activity (Martin & Vagelos, 1962); therefore, the elevated malonyl-CoA may be caused by accumulated citrate. Consistently, we have showed that TFAM knockdown in HCC cells increased ACC activity and the intracellular contents of neutral lipids (Fig EV4B and C). In addition, the enhanced glycolysis, as evidenced by the increased intracellular lactate level and extracellular acidification rate (ECAR), was observed in HCC cells after treatment with TFAM knockdown (Fig 7B and C).

To directly test whether these metabolites induce PTMs and are involved in the nuclear translocation of mDia2, we performed an immunoprecipitation (IP) assay to purify mDia2 from HCC cells (Fig EV4D). The purified mDia2 protein was then subjected to Western blotting using antibodies targeting specific PTMs, which revealed that malonylation was the most significantly increased PTM of mDia2 in HCC cells with TFAM deficiency (Figs 7D and EV4E). Increased levels of malonylated mDia2 were also observed in the nuclear fraction of TFAM-knockdown HCC cells (Figs 7E and EV4F). Next, we tested whether malonyl-CoA levels affected malonylation of mDia2 in HCC cells. As shown in Figs 7F and EV4G–L, malonyl-CoA incubation significantly increased the level of intracellular malonyl-CoA, malonylated mDia2 and its nuclear translocation. In contrast, reduced intracellular malonyl-CoA, caused by the inhibition (or knockdown) of ACC1, which carboxylates acetyl-CoA to form malonyl-CoA, exerted the opposite effect. Importantly, we found that the inhibition (or knockdown) of ACC1 significantly impeded *in vitro* migration of HCC cells, the spread in mice and prolonged their lifespan (Figs 7G–J and EV4 M and N). To further investigate the effects of malonylation of mDia2 on metastasis, SIRT5, the most important demalonylation enzyme (Peng *et al*, 2011), was overexpressed in TFAM-knockdown cells (Fig EV5A). As shown in Fig EV5B, D and F, SIRT5 overexpression significantly decreased the level of malonylated mDia2 and nuclear-located mDia2 and inhibited the migration and invasion of SNU-368 shTFAM cells. Consistently, knockdown of SIRT5 with siRNA (Fig EV5A) or treatment with the SIRT5 inhibitor NRD167 significantly reversed the effect of SIRT5 overexpression on the malonylation of mDia2 and the migration and invasion of HCC cells (Fig EV5C, E and G).

Previous studies have reported that the post-translational modifications (PTM) in nuclear localization sequence (NLS) domain significantly affects the nuclear import of proteins (Li *et al*, 2012; An *et al*, 2017). Since only two lysine residues (12 and 27), which is the most studied residue with PTM (Peng *et al*, 2011), exist in the NLS region of mDia2, we speculated that both of them have the potential to be malonylated and affect mDia2 nuclear translocation. Therefore, we generated K12E and K27E mutants to mimic malonylation. Additionally, K12Q and K27Q acetylation-mimetic mutants were also generated. Both were unable to undergo malonylation and acted as controls. Our results demonstrated that only the K27E mutant significantly promoted nuclear translocation of mDia2 and nuclear actin polymerization in HCC cells with endogenous mDia2 knockdown (Fig 7K and L and Appendix Fig S5A–C), suggesting that malonylation of K27 on mDia2 may play a critical role in the nuclear translocation process. More importantly, the K27E mutant strongly induced HCC cell migration and invasion (Fig 7M and

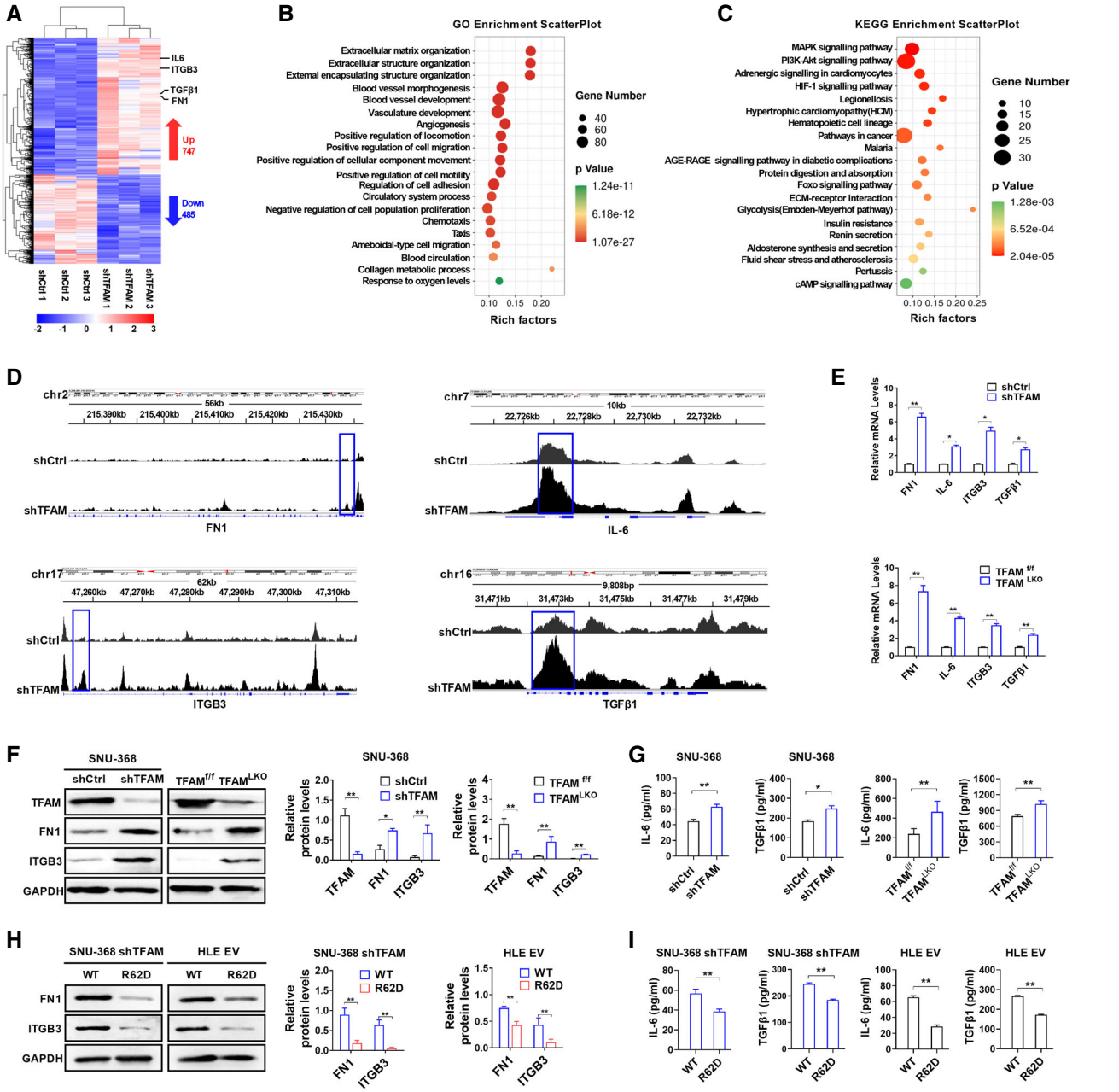

Figure 5. Downregulated TFAM induced the expression of metastatic genes in a nuclear F-actin-dependent way.

A Expression heatmap of ATAC-DEGs in TFAM knockdown and control SNU-368 cells (n = 3 per group). Up- and down-regulated ATAC-DEGs in TFAM knockdown HCC cells were annotated.

B, C Top 20 GO terms and enriched KEGG pathways enriched by ATAC-DEGs. Rich factor represents the ratio of the number of mapped genes to the number of all the annotated genes located in the pathway.

D ATAC-seq signal tracks around the FN1, IL-6, TGFB1, and ITGB3 genes in HCC cells with treatment as indicated. Blue box indicates promoter region with increased accessibility.

E, F qRT–PCR and Western blot assays for mRNA and protein expression levels of metastasis-related gene in HCC cells (n = 3 independent experiments) and tumor tissues from mice (n = 4 per group) with treatments as indicated.

G ELISA for the levels of IL-6 and TGFB1 in HCC cells and tumor tissues from mice with treatments as indicated (n = 3 independent experiments).

H, I Western blot assays and ELISA for the levels of FN1, IL-6, TGFB1, and ITGB3 in HCC cells with treatment as indicated (n = 3 independent experiments).

Data information: Graphs show mean ± SEM, two-tailed unpaired t-test. *P < 0.05; **P < 0.01.
Source data are available online for this figure.

Appendix Fig S5D). Next, we focused on the mechanism underlying nuclear translocation via the importin complex. Treatment with ivermectin, an inhibitor of importin α/β-dependent nuclear import, reduced the levels of nuclear mDia2 (Appendix Fig S5E). We also observed that the K27E mutant from shCtrl cells specifically interacted with importin α1 in HCC cells, whereas the K27Q mutant from shTFAM cells failed to interact, suggesting that K27 malonylation is likely critical for this interaction (Appendix Fig S5F).

Downregulation of TFAM and nuclear F-actin was associated with poor prognosis in HCC patient

TFAM expression was further analyzed using 429 paired HCC tissues by IHC and RNA-seq data from TCGA database, which included 50 paired HCC tissue samples. Our results indicated that TFAM expression was decreased in 66.7% (286 out of 429) of HCC patients at the protein level and in 40.0% (20 out of 50) of HCC patients at

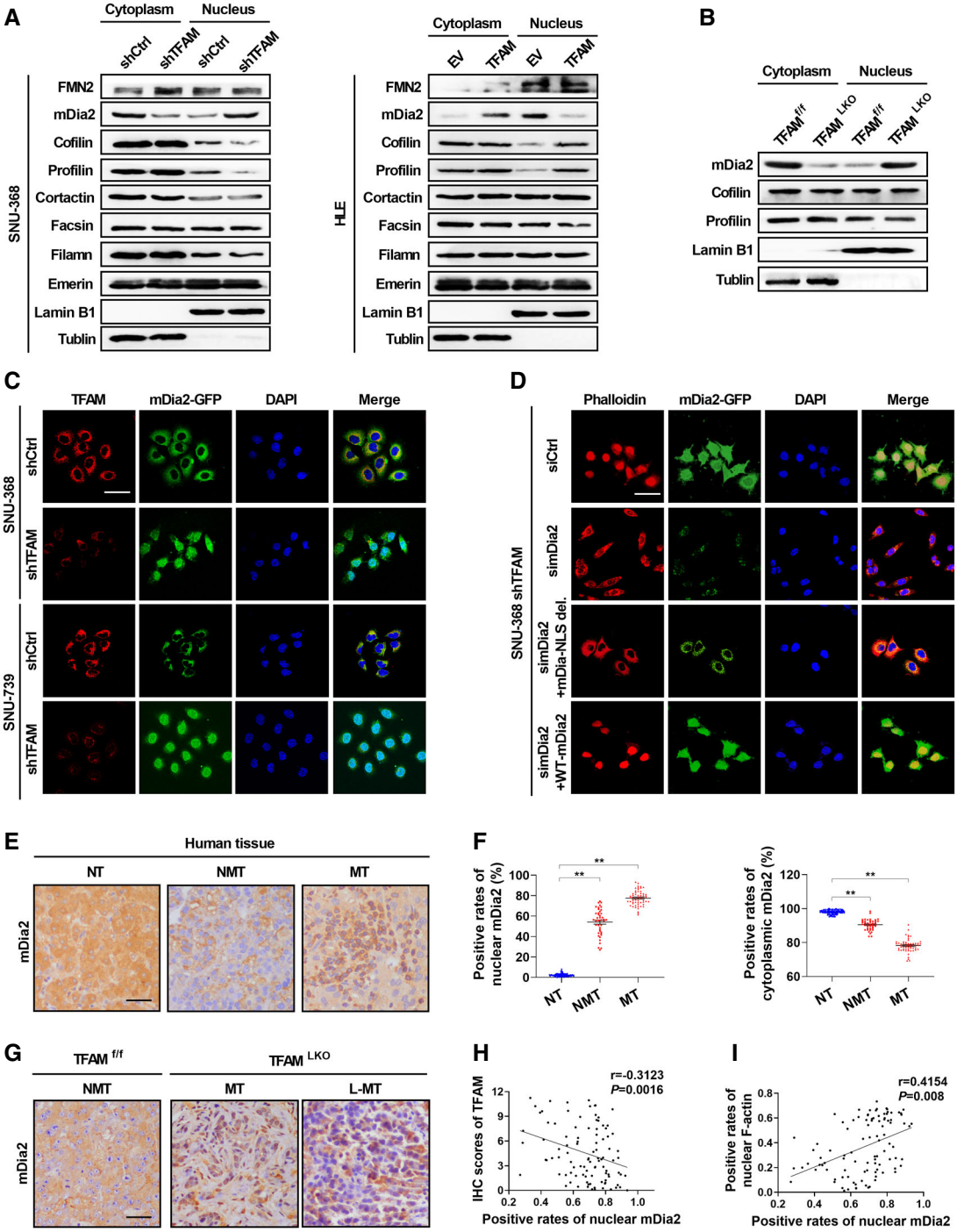

Figure 6.

Figure 6. Downregulated TFAM induced nuclear translocation of mDia2 to promote nuclear actin polymerization.

A Western blot analyses for the protein level of key regulators of actin polymerization in the cytoplasm and nucleus of HCC cells with treatment as indicated. Tublin and Lamin B1 were used as loading controls for the cytoplasm and nucleus, respectively (n = 3 independent experiments).

B Western blot analyses for the protein level in tissues of mouse liver tumor induced by Akt/β-catenin (n = 3 independent experiments).

C Representative immunofluorescence images of HCC cells co-transfected with mDia2-GFP and other constructs as indicated (n = 3 independent experiments). Scale bars, 20 μm.

D Representative images of immunofluorescence assay for mDia2 and phalloidin staining for HCC cells with treatment as indicated (n = 3 independent experiments). WT-mDia2: expression vector encoding wild type mDia2. mDia2-NLS del.: expression vector encoding truncated mDia2 lacking NLS peptide. Scale bars, 20 μm.

E–G Representative IHC images of mDia2 nuclear translocation in human (E) and mouse (G) HCC tissues. NT, non-tumor liver tissues, n = 100; MT, metastatic tumor tissues, n = 58; NMT, non-metastatic tumor tissues n = 42. Scale bars, 25 μm. (F) Positive rates of mDia2 in nucleus and cytoplasm was calculated based on the IHC assay in (E). Graphs show mean ± SEM. One-way ANOVA. $^{**}P < 0.01$.

H, I Spearman correlation analysis between the positive rates of nuclear mDia2 and the TFAM expression level (or positive rates of nuclear F-actin) based on the IHC assay in (E).

Source data are available online for this figure.

the mRNA level when compared with the paired adjacent non-tumor liver tissues (Fig 8A and B). We used the HCC subclass with downregulated TFAM in subsequent experiments. Since it was reported that alterations in gene expression profiles favoring HCC metastasis were initiated in primary tumors (Ye *et al*, 2003; Roessler *et al*, 2015), the expression of TFAM was further compared between metastatic (n = 228) and non-metastatic (n = 58) HCC tissues. Our data demonstrated that metastatic HCC tissues exhibited significantly lower TFAM expression levels than non-metastatic HCC tissues (Fig 8C). As expected, TFAM expression was significantly associated with overall survival and time to tumor recurrence (Fig 8D and E). These findings further imply that the downregulation of TFAM plays an important role in HCC metastasis. Consistently, the positive rates of nuclear F-actin were also found to be significantly associated with overall survival and time to tumor recurrence in HCC patients (Fig 8F and G). Moreover, our results demonstrated that the expression levels of TFAM in HCC tissues were negatively associated with the levels of four metastatic genes (FN1, IL-6, TGFβ, and ITGB3), which were shown to be regulated by nuclear F-actin (Fig 8H and I).

Discussion

Experimental HCC models with metastasis are essential for exploring the mechanism of HCC metastasis and elucidating contributing factors. However, xenograft mouse models, the most widely used strategy, can only be carried out in immunodeficient mice, the immunological environment of which is very different from that in patients. Therefore, establishing an effective and reliable spontaneous HCC mouse model with metastasis is urgently required. In the present study, three mitochondrial genes were chosen to induce spontaneous lung metastasis in mouse liver cancer models. Interestingly, only $TFAM^{LKO}$ mice rapidly and stably developed lung metastases, suggesting that mitochondrial dysfunction induced by TFAM loss, but not by deregulation of mitochondrial morphology, has a strong ability to drive tumor metastasis. As the key regulator of mtDNA replication and transcription, TFAM has been reported to be deeply involved in metabolic reprogramming and proliferation of tumor cells (Woo *et al*, 2012; Huang *et al*, 2014; Yang *et al*, 2021). Moreover, TFAM expression is a prognostic factor for survival in endometrial carcinomas and colorectal cancer patients with tumor

Figure 7. Downregulated TFAM induced malonylation of mDia2 to promote its nuclear translocation.

A Schemes of glucose metabolism alternation detected by targeted metabolomics. The fold change of metabolites in mitochondria and cytoplasm between TFAM knockdown and WT SNU-368 cells were shown (n = 6 per group). Increased and decreased metabolites are indicated by red and green circles, respectively.

B The fold change of intracellular acetyl-CoA, malonyl-CoA, and lactate in SNU-368 cells with TFAM knockdown was evaluated by ELISA or enzymatic reaction (n = 3 independent experiments).

C Extracellular acidification rate (ECAR) was measured in TFAM knockdown and WT SNU-368 cells with serial addition of glucose, oligomycin and 2-DG (n = 3 independent experiments). The panel shows the calculated glycolytic parameters, including glycolysis and maximal glycolysis. Glycolysis was calculated as maximum rate measurement before Oligomycin injection minus last rate measurement before glucose injection. While glycolytic capacity was calculated as maximum rate measurement after Oligomycin injection minus last rate measurement before glucose injection.

D Western blot analysis of anti-mDia2 IPs and whole-cell lysates (WCL) derived from HCC cells and mouse tumor tissues (n = 3 independent experiments). NT, non-tumor liver tissues; MT, metastatic tumor tissues; NMT, non-metastatic tumor tissues.

E The level of malonylated mDia2. Equal amount of immunoprecipitated mDia2 either from TFAM knockdown or control cells was loaded in Western blot assay.

F Western blot analysis for the distribution of mDia2 in SNU-368 cells incubated with malonyl-CoA (5 μM) or ND-630 (10 μM) (n = 3 independent experiments).

G Bioluminescent images for lung metastasis in mice inoculated with HCC cells. n = 10. Ten days after orthotopic implantation of SNU-368 shTFAM cells, ND-630 (3 mg/kg) was intravenously injected in mice every 2 days until euthanasia was performed.

H Representative H&E images of lung metastasis in mice used in (G). Scale bars, 100 μm.

I Number of metastatic nodules per lung in mice used in (G).

J Kaplan–Meier survival curves for mice inoculated with orthotopic HCC cells as indicated. n = 10 per group.

K, L Representative merged images of mDia2-GFP (Green) and DAPI staining (blue) (K) and Phalloidin (Red) and DAPI staining (blue) (L) in HCC cells transfected with different mutant mDia2-GFP constructs as indicated (n = 3 independent experiments). Scale bars, 20 μm. K12E and K27E are malonylation-mimetic mutants at lysine residues 12 and 27. K12Q and K27Q are acetylation-mimetic mutants at lysine residues 12 and 27.

M Statistical analysis of transwell migration and invasion assays for HCC cells with treatment as indicated (n = 3 independent experiments).

Data information: Graphs show mean ± SEM, two-tailed unpaired t-test for (B, C, I). One-way ANOVA for (M). $^{*}P < 0.05$; $^{**}P < 0.01$.
Source data are available online for this figure.

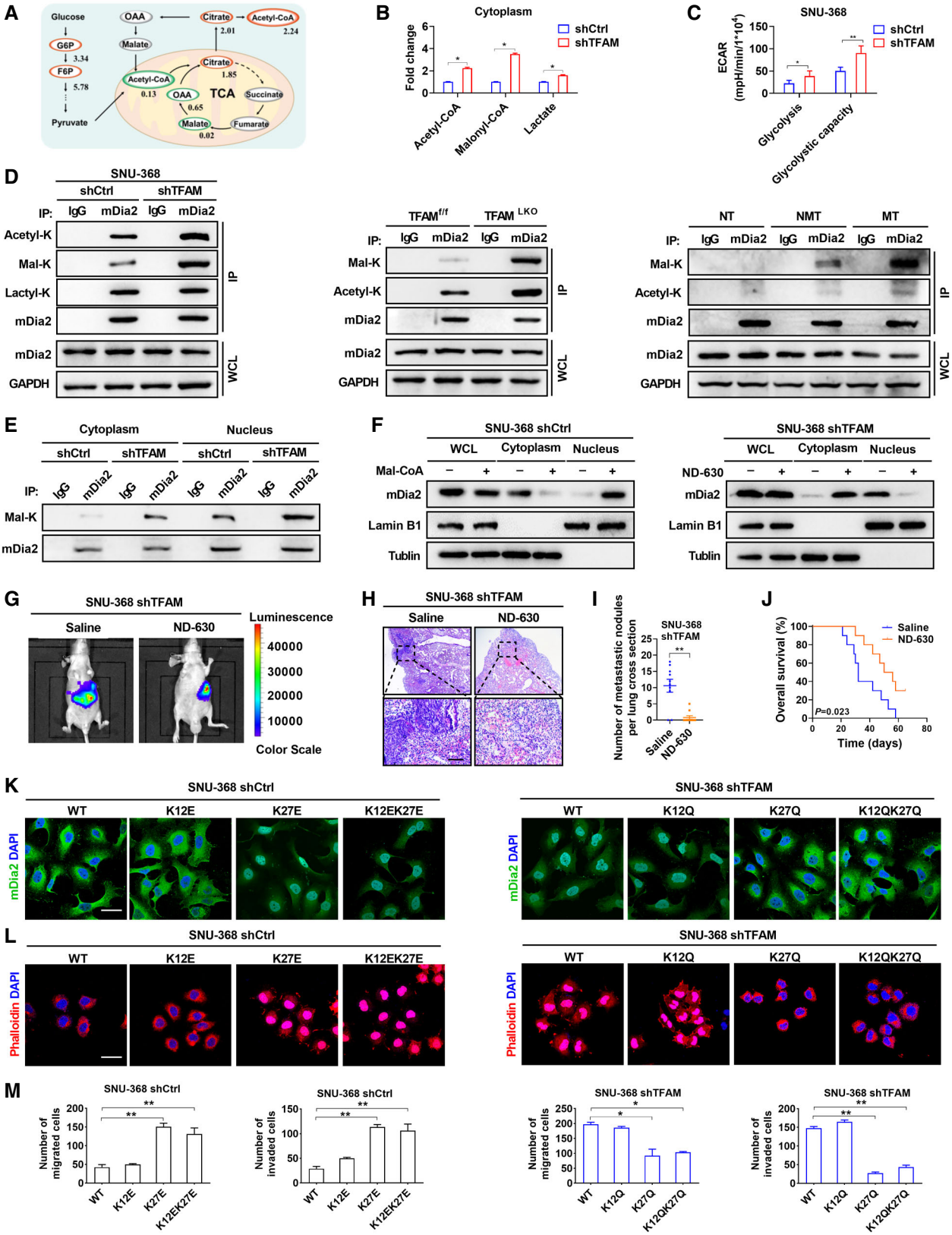

Figure 7.

metastasis (Toki *et al*, 2010; Yoshida *et al*, 2011). Consistently, in the present study, we showed that TFAM expression was significantly downregulated, especially in metastatic HCC tissues, and was associated with HCC recurrence. However, the TFAM protein was detectable in most non-metastatic HCC tissues. Therefore, stimulation of TFAM expression or blockage of TFAM degradation may be

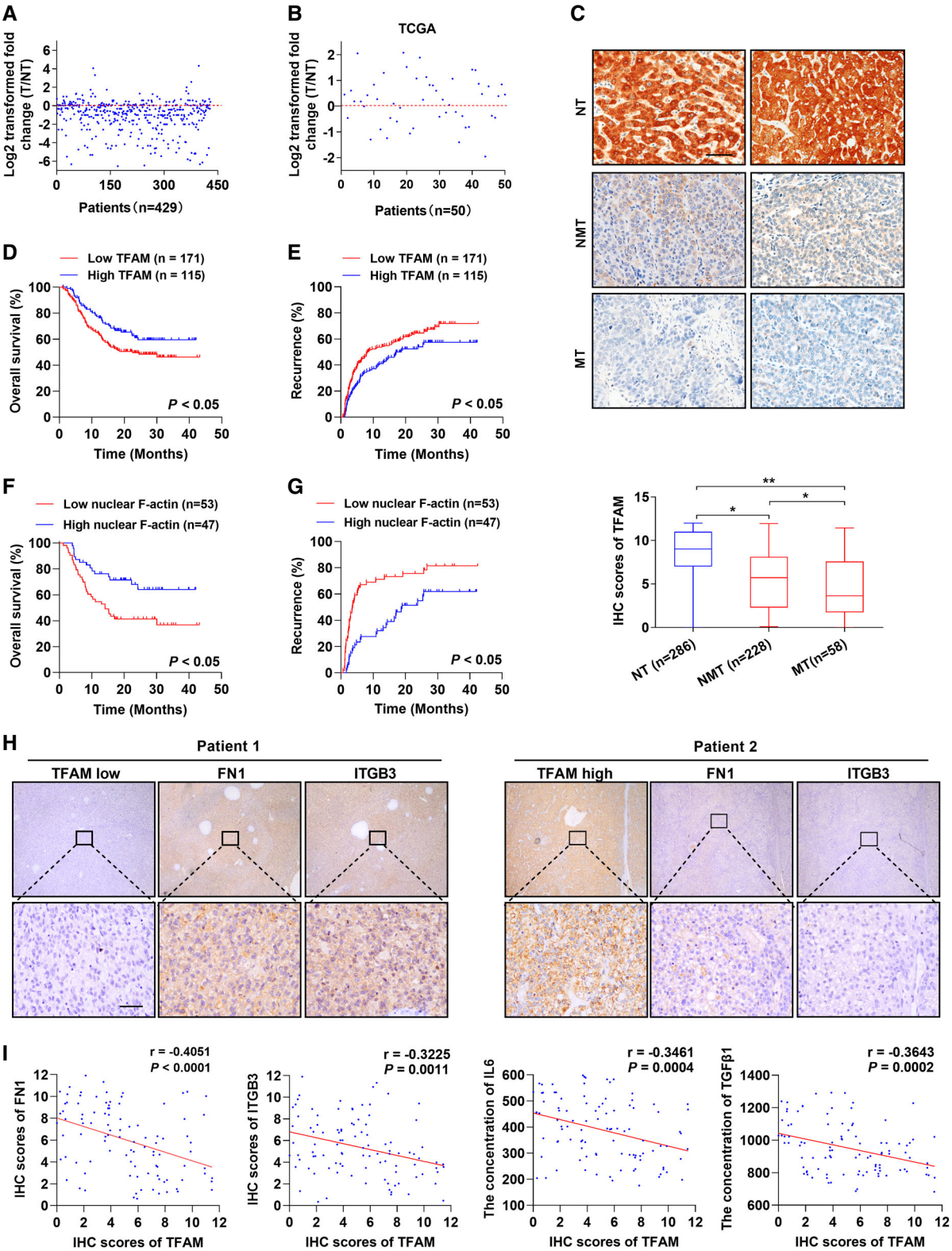

Figure 8.

Figure 8. Downregulation of TFAM and nuclear F-actin were associated with poor prognosis in HCC patient.

A IHC scores of TFAM in 429 paired tissues from HCC patients. The relative expression ratio of tumor to non-tumor was log2-transformed. T, tumor tissues; NT, non-tumor liver tissues.

B mRNA level of TFAM in 50 HCC patients' paired tissues from TCGA database. The relative expression ratio of tumor to non-tumor was log2-transformed.

C Representative images of IHC staining of TFAM (top panel) and scores (bottom panel) in HCC tumor tissues. One-way ANOVA. *$P < 0.05$; **$P < 0.01$. MT, metastatic tumor tissues; NMT, non-metastatic tumor tissues. Scale bars, 25 μm. Boxes: first quartile to third quartile; Whiskers: minimum value to maximum value; Central band: median.

D, E Kaplan–Meier curves for overall survival and the recurrence of HCC patients stratified by TFAM expression.

F, G Kaplan–Meier curves for overall survival and the recurrence of HCC patients stratified by nuclear F-actin positive rates.

H Representative images of IHC staining of TFAM, FN1, and ITGB3 from two HCC patients. Scale bars, 25 μm.

I Spearman correlation analysis between the levels of TFAM and FN1, IL-6, TGFB1, or ITGB3.

a potential strategy to prevent metastasis in HCC. For example, the experimental drug LY379268 was reported to upregulate the expression of TFAM and prevent diabetic peripheral neuropathy by improving mitochondrial function in dorsal root ganglion neurons (Chandrasekaran *et al*, 2017). In addition, etramethylpyrazine, a natural small molecule compound, was found to stabilize TFAM by directly interacting with TFAM, which blocked Lon protease access and thus decreased TFAM degradation (Lan *et al*, 2017).

This metastasis-promoting effect of TFAM loss was strongly supported by both RNA-Seq and ATAC-seq, which showed that GO terms such as ECM remodeling, angiogenesis, cell migration, and adhesion were enriched. To partially support this finding, Fu *et al* found that TFAM-deficient regulatory T cells exhibited deregulated cell adhesion and regulation of the actin cytoskeleton (Fu *et al*, 2019). The HIF-1/SNHG1/miR-199a-3p/TFAM axis also regulates tumor angiogenesis and metastasis under hypoxic conditions in breast cancer (Zuo *et al*, 2021). Importantly, four key players in metastasis were screened and verified as downstream targets of TFAM. The ECM protein FN1, an epithelial-to-mesenchymal transition marker, was reported to promote the migration and invasion of HCC and other cancer cells (Xu *et al*, 2015). Interestingly, signals that control these metastatic behaviors are transmitted from FN1 to the cell by integrins, a family of transmembrane receptors. One of the major integrins, ITGB3, was also induced by TFAM loss and was shown to dramatically promote angiogenesis and the metastatic ability of tumor cells (Huang & Rofstad, 2018). Additionally, TGF-β and IL-6, which have been implicated in many metastatic processes, were also identified, providing strong evidence to explain TFAM deficiency-mediated metastasis.

TFAM is necessary for transcription and replication of mtDNA, which encodes proteins involved in electron transport chain (ETC), whose defects always induce extensive metabolic changes in TCA cycle. Previously, we found that TFAM plays a crucial regulatory role in mitochondrial energy metabolism in tumor cells (Huang *et al*, 2014; Wen *et al*, 2019; Yang *et al*, 2021). In addition, previous studies have also reported the role of TFAM deficiency in disturbing TCA cycle. For example, TFAM knockdown in human erythroid (K562) cells decreased the level of malate, alpha-ketoglutarate, and acetyl-CoA(Liu *et al*, 2017), while skeletal muscle-specific overexpression of TFAM induced an increase in malate, citrate, and other TCA cycle metabolites when compared with WT mice(Koh *et al*, 2019). However, the underlying mechanism is far from clear. In the present study, we observed a roadblock in the TCA cycle induced by TFAM knockout. Interestingly, this blockage did not simply induce an overall reduction in metabolites involved in the TCA cycle. Instead, it caused the accumulation of citrate in the mitochondria and cytoplasm, as well as increased levels of cytoplasmic acetyl-CoA and its derivative malonyl-CoA. We speculated that loss of TFAM in HCC cells leads to functional defects in the electron transport chain, which blocks the TCA cycle. Similarly, the TCA cycle roadblock induced by the deficiency of enzymes in the TCA cycle, such as succinyl-CoA ligase, also leads to the reversal of substrate flow and increased citrate and acetyl-CoA in human T cells (Wu *et al*, 2020).

The biological significance of lysine malonylation, a newly identified protein post-translational modification, remains poorly understood. In particular, its potential role in human cancers remains largely unknown. In the present study, we found that metabolic reprogramming induced by TFAM deficiency significantly promoted the malonylation of NLS in mDia2, facilitating its interaction with importin α1 and subsequent nuclear translocation. This is consistent with a previous study that showed that the NLS of mDia2 binds to importin α and is imported into the nucleus by the importin α/β complex (Miki *et al*, 2009). In fact, through the reversible addition of a malonyl group to lysine residues, the changed charge may alert electrostatic interactions and protein conformation and also lead to alerted protein interactions. For example, following LPS treatment, malonylated GAPDH directly interacts with various ribosomal components (Galván-Peña *et al*, 2019). Similarly, protein phosphorylation generates a −1 charge and enhances its nuclear import (Nardozzi *et al*, 2010). For instance, it has been shown that phosphorylation of Ser^{385} in the EBV nuclear antigen 1 (EBNA-1) NLS upregulates its nuclear transport by increasing the binding affinity for the import adaptor importin α5 (Sugden & Warren, 1989).

mDia2, a formin protein, is an actin nucleation and elongation factor that assembles into linear actin filaments. The present study found that the nuclear localization of mDia2 induced by TFAM knockdown significantly promoted nuclear actin polymerization in HCC cells. In line with these findings, Baarlink *et al* (2013) reported that serum stimulates rapid assembly of F-actin within the nucleus in an mDia2-dependent manner in mouse embryonic fibroblast cells (NIH3T3). Moreover, the polymerization of nuclear actin has also been observed in NIH3T3 cells during cell spreading (Plessner *et al*, 2015). Notably, a previous study showed that polymerization of nuclear actin allows chromatin compaction to be reordered to access genetic loci for transcription or repair (Baarlink *et al*, 2017). Specific inhibition of nuclear F-actin assembly impairs nuclear expansion and chromatin decondensation in NIH3T3 cells (Baarlink *et al*, 2017). Similarly, our work showed that polymerized nuclear actin significantly induced the expression of metastatic genes. However, the most significant impact of TFAM-mediated chromatin accessibility on metastatic gene expression is poorly understood and requires further investigation.

In summary, this work shows that TFAM knockout rapidly and stably induces spontaneous lung metastasis in mouse liver cancer models. TFAM expression was significantly downregulated in metastatic HCC tissues and associated with overall survival and time to tumor recurrence. Importantly, we showed that TFAM deficiency-driven metastasis is dependent on the polymerization of nuclear actin, which modulates chromatin accessibility and coordinates the expression of metastatic genes. Mechanistically, TFAM deficiency blocked the tricarboxylic acid cycle and increased intracellular malonyl-CoA levels. Malonylation of mDia2 promotes nuclear translocation and the subsequent polymerization of nuclear actin. Our study connects mitochondria to the metastasis of human cancer by uncovered mitochondria-to-nucleus retrograde signaling, indicating that TFAM may serve as an effective molecular target to block HCC metastasis.

Materials and Methods

Reagents and antibodies

Diethylnitrosamine (DEN, Cat. No. 73861), CCl_4 (Cat. No. 1601168), and malonyl coenzyme A lithium salt (Cat. No. 685518) were purchased from Sigma-Aldrich (St. Louis, MO). Actin-stain™ 555 fluorescent phalloidin (Cat. No. PHDH1-A) was purchased from Cytoskeleton Inc. (Denver, CO, USA). Acetyl CoA carboxylase (ACC) inhibitor Firsocostat (ND-630, Cat. No. HY-16901A) and importin α/β inhibitor ivermectin (Cat. No. HY-15310) were purchased from MedChemExpress (Newark, NJ). SIRT5 inhibitor NRD167 (Cat. No. S9903) was purchased from Selleck Chemicals (Houston, TX). The primary antibodies used in this study and their working concentrations are listed in Table 1.

Table 1. Primary antibodies used for Western blot, immunohistochemistry, and immunoprecipitation.

Antibody	Company (Cat. No.)	Working concentration dilutions
TFAM	Novus (NBP2-19437)	IP: 5 μg/μl
TFAM	Abcam (ab176558)	WB: 1/1,000, IHC: 1/200, IF:1:250
DIAPH3	Abcam (ab245660)	WB: 1/1,000, IF:1/200
DIAPH3	Proteintech (14342-1-AP)	WB: 1/1,000, IF:1/200, IHC: 1/200
DIAPH3	Novus (NBP2-80419)	IP: 5 μg/μl
GAPDH	Cell Signaling (#5174)	WB: 1/2,000
FMN2	Proteintech (11259-1-AP)	WB: 1/1,000
Cofilin	Cell Signaling (#5175)	WB: 1/1,000
Profilin 1	Abcam (ab124904)	WB: 1/10,000
Cortactin	Proteintech (11381-1-AP)	WB: 1/1,000
Fascin	Abcam (ab126772)	WB: 1/1,000
Filamin	Novus (NB600-1218)	WB: 1/1,000
Emerin	Cell Signaling (#30853)	WB: 1/1,000
Import α1	Abcam (ab70160)	WB: 1/1,000
Lamin B1	Proteintech (12987-1-AP)	WB: 1/1,000
Importin β1	Cell Signaling (#51186)	WB: 1/1,000
Integrin β3	Cell Signaling (#13166)	WB: 1/1,000
IgG (H + L)	Cell Signaling (#14708)	IP: 5 μg/μl
Rabbit IgG	Cell Signaling (#2729)	WB: 1/1,000
Mouse IgG	Beyotime (A7028)	WB: 1/1,000
Fibronectin	Abcam (ab2413)	WB: 1/1,000
Actin	Abcam (ab179467)	WB: 1/3,000, IP: 5 μg/μl
Mono/di-meMRmethylysine	PTM Bio (PTM-602)	WB: 1/1,000
Phosphotyrosine	PTM Bio (PTM-701)	WB: 1/1,000
O-GlcNAc	PTM Bio (PTM-952)	WB: 1/1,000
Acetyllysine	PTM Bio (PTM-102)	WB: 1/1,000
L-lactyl Lysine	PTM Bio (PTM-1401RM)	WB: 1/1,000
Malonyllysine	PTM Bio (PTM-902)	WB: 1/1,000
Succinyllysine	PTM Bio (PTM-401)	WB: 1/1,000
SIRT 5	Proteintech (67257-1-Ig)	WB: 1/2,000
ACC1	Proteintech (21923-1-AP)	WB: 1/1,000
Tubulin	Abcam (ab7291)	WB: 1/1,000

Cell culture and tissue collection

Human HCC cells SNU-739 and SNU-368 were purchased from the Korean Cell Line Bank (Seoul, Republic of Korea), JHH-2, HLF, and HLE were purchased from the Japanese Collection of Research Bioresources Cell Bank (Osaka, Japan), and LM3, MHCC-97H, Hep3B, Huh7, and Huh6 were maintained in our laboratory. Immortalized liver cells LO2 were purchased from the Institute of Biochemistry and Cell Biology, Chinese Academy of Sciences (Shanghai, China). The cells were cultured in RPMI-1640 medium (Gibco, Thermo Fisher Scientific, Inc., Waltham, MA) or Dulbecco's modified Eagle's medium (DMEM, Gibco). All HCC cell lines were authenticated using short tandem repeat DNA testing by the FMMU Centre for DNA Typing and were tested mycoplasma negative. In addition, 429 tissue samples from patients with HCC were collected at Xijing Hospital affiliated with the Fourth Military Medical University (FMMU) in Xi'an, China (Table 2). All participants provided written informed consent, and the study was approved by the ethics committee of the FMMU (KY20213188-1).

Experimental animals

C57BL/6-*TFAM*$^{flox/flox}$ mice (LoxP sites flanking exons 6–7 of *TFAM*), C57BL/6-*MFN1*$^{flox/flox}$ mice (Loxp sites flanking exon 4 of *MFN1*), and C57BL/6-*MFN2*$^{flox/flox}$ mice (Loxp sites flanking exon 6 of *MFN2*) were generously gifted by Professor Yongzhan Nie (Department of Digestive Diseases, Xijing Hospital, FMMU). Alb-Cre mice were purchased from Shanghai Model Organisms Center, Inc. (Shanghai, China). Mice with liver-specific knockout of *TFAM*, *MFN1*, or *MFN2* were generated by crossing floxed mice with Alb-Cre mice under specific pathogen-free (SPF) conditions at the laboratory animal center of FMMU. The genotypes of the mice were evaluated using multiplex PCR and agarose gel electrophoresis. The primers used are shown in Table 3.

Sleeping beauty (SB)-mediated hydrodynamic injection was performed as described previously (Chen & Calvisi, 2014). The plasmids used in this model, including pT3-EF1α-HA-myr-Akt,

Table 2. Clinical characteristics of HCC patients.

Variables	No. of cases
Total	429
Age, years	
<54	222
≥54	207
Gender	
Female	57
Male	372
HBsAg	
Negative	38
Positive	391
AFP, ng/ml	
<200	247
≥200	182
HCC size, cm	
<5	174
≥5	255
Tumor number	
Single	344
Multiple	85
Differentiation	
I+II	151
III+IV	278
TNM	
I+II	357
III+IV	72
PVTT	
Negative	387
Positive	42
Adjuvant therapy	
No	319
TACE	110
Survival	
Alive	298
Dead	131
Relapse	
No	180
Yes	249

Abbreviations: AFP, alpha-fetoprotein; TNM, tumor-node-metastasis; PVTT, portal vein tumor thrombus.

pT3-EF1α-ΔN90-β-catenin, pT2CAGGS-NRasV12, and pCMV/SB transposase, were generously gifted by Prof. Xin Chen (University of California, San Francisco) and have been described previously in detail (Wang *et al*, 2015; Qiao *et al*, 2018). Wild-type (not injected, Appendix Fig S1C) and mice injected with pT3-EF1α empty plasmid were used as controls (Appendix Fig S2B).

For chemically induced HCC, male mice aged 14 days were given a single intraperitoneal (i.p.) injection of DEN (25 mg/kg) and subsequent weekly injections of CCl_4 (4 weeks after DEN, 2.5 ml/kg, 1:4 diluted with olive oil, i.p.). The xenograft mouse model was established using HCC cells and male BALB/c nude mice as previously described (Huang *et al*, 2016). Ten days after orthotopic implantation of HCC cells, ND-630 (3 mg/kg) was intravenously injected in mice every 2 days. In the xenograft study, the maximum allowable size is 20 mm in diameter. The animal study was approved by the Ethics Committee of the Fourth Military Medical University for animal research (IACUC-20170105). No specific method was used to predetermine sample size. Exclusion criteria have been established in advance for animal studies (i.e., animals with sickness or significant weight differences will be excluded). In this study, animals which died during modeling were excluded.

Knockdown and forced expression of target genes

Lentiviruses for TFAM, MFN2 knockdown and TFAM, SIRT5 overexpression were prepared as previously reported (Yang *et al*, 2021). Plasmids encoding nuclear-located WT actin (Cat. No. 118380) and the mutant R62D (Cat. No. 118381) were obtained from Addgene and reconstructed by Tsingke Biotechnology Co., Ltd. (Beijing, China) to fuse GFP to the carboxyl terminus. Plasmids encoding WT and mutant mDia2 were also constructed by Tsingke Biotechnology Co., Ltd. All siRNAs were synthesized by GenePharma (Shanghai, China). The siRNA sequences are listed in Appendix Table S3. The siRNAs were transfected with Lipofectamine 2000 reagent (Cat. No. 11668019, Invitrogen, CA) according to the manufacturer's instructions.

Immunoprecipitation, Western blot, and immunohistochemistry

The Pierce Classic Magnetic IP/Co-IP Kit (Cat. No. 88805, Thermo Fisher Scientific, MA) was used for IP. Briefly, HCC cells or fresh mouse liver tumor tissues were lysed with IP lysis buffer (phosphatase inhibitor cocktail and protease inhibitor cocktail were added before use). The protein sample was immunoprecipitated with 5–10 μg of antibody overnight at 4°C. Subsequently, 20–40 μl of fully suspended protein A/G magnetic beads were added and incubated at room temperature for 1.5 h. The complexes that bound to the protein A/G conjugate were washed and subjected to Western blot.

HCC tissues and cell lines were processed for Western blot as previously described (Ji *et al*, 2021). Western blot was then analyzed for band intensity with ImageJ software (National Institutes of Health, MD). For IHC, the expression level of target proteins was independently evaluated by two pathologists who were blinded to the clinical data, according to the proportion and intensity of positive cells that were determined within five microscopic visual fields per slide (200-fold magnification). A proportion score, which represents the estimated proportion of positively stained tumor cells, was assigned as previously described(Lutz-Bonengel *et al*, 2021).

Quantitative Real-Time (qRT) Polymerase Chain Reaction (PCR)

Total RNA from HCC tissues or cells was extracted using RNAiso Plus (Cat. No. 9109, Takara, Tokyo, Japan). Complementary DNA (cDNA) was generated from total RNA (500 ng) using the

Table 3. Sequence of primers for qRT–PCR analysis.

Gene	Forward Primer	Reverse Primer
3.1 Primers used in qPCR analysis		
TFAM	ATGGCGTTTCTCCGAAGCAT	TCCGCCCTATAAGCATCTTGA
GAPDH	GGAGCGAGATCCCTCCAAAAT	GGCTGTTGTCATACTTCTCATGG
TGF-β	AAGGACCTCGGCTGGAAGTGC	CCGGGTTATGCTGGTTGTA
IL-6	AATAACCACCCCTGACCCAAC	ACATTTGCCGAAGAGCCCT
FN1	ACCAACCTACGGATGACTCG	GCTCATCATCTGGCCATTTT
ITGB3	GTGAGTGCGATGACTTCTCCTG	CAGGTGTCAGTGCGTGTAGTAC
Actin-NLS	AGAAAAAGCGGAAGGTGGGA	AATCCTTCTGACCCATGCCC
Gene	**Forward**	**Reverse**
3.2 Primers for genotyping		
TFAM	CTGCCTTCCTCTAGCCCGGG	GTAACAGCAGACAACTTGTG
MFN1	AGCAGTTGGTTGTGTGACCA	TTGGTAATCTTTAGCGGTGCTC
MFN2	GAAGTAGGCAGTCTCCATAG	AACATCGCTCAGCCTGAACC
Alb-cre	TGGCAAACATACGCAAGGG	CGGCAAACGGACAGAAGCA
Gene		**siRNA target sequence**
3.3 SiRNA		
siCtrl		UUCUCCGAACGUGUCACGUTT
simDia2		CAUCGCCUUGAAGAUAUUATT
siACC1		GAAGGTTCTTATCGCCAACAA
siSIRT 5		GCUGAAUUUAACACGGAGA
3.4 Targeted sequence of point mutations Plasmid		
mDia2-WT	ctcgagATGAGTGAGGAGAGGAGCCTTTCCTTATTGGCCAAAGCCGTGGATCCCAGACACCCCAATATGATGACAGA TGTGGTTAAACTTCTCTCTGCGGTATGCATTGTAGGGGAAGAAAGCATCCTTccaccggt	
mDia2-K12R	ctcgagATGAGTGAGGAGAGGAGCCTTTCCTTATTGGCCAGAGCCGTGGATCCCAGACACCCCAATATGATGACAG ATGTGGTTAAACTTCTCTCTGCGGTATGCATTGTAGGGGAAGAAAGCATCCTTccaccggt	
mDia2-K27R	ctcgagATGAGTGAGGAGAGGAGCCTTTCCTTATTGGCCAAAGCCGTGGATCCCAGACACCCCAATATGATGACAGA TGTGGTTAGACTTCTCTCTGCGGTATGCATTGTAGGGGAAGAAAGCATCCTTccaccggt	
mDia2-K12R-K27R	ctcgagATGAGTGAGGAGAGGAGCCTTTCCTTATTGGCCAGAGCCGTGGATCCCAGACACCCCAATATGATGACAGAT GTGGTTAGACTTCTCTCTGCGGTATGCATTGTAGGGGAAGAAAGCATCCTTccaccggt	
mDia2-K12Q	ctcgagATGAGTGAGGAGAGGAGCCTTTCCTTATTGGCCCAGGCCGTGGATCCCAGACACCCCAATATGATGACAGAT GTGGTTAAACTTCTCTCTGCGGTATGCATTGTAGGGGAAGAAAGCATCCTTccaccggt	
mDia2-K27Q	ctcgagATGAGTGAGGAGAGGAGCCTTTCCTTATTGGCCAAAGCCGTGGATCCCAGACACCCCAATATGATGACAGAT GTGGTTCAGCTTCTCTCTGCGGTATGCATTGTAGGGGAAGAAAGCATCCTTccaccggt	
mDia2-K12Q-K27Q	ctcgagATGAGTGAGGAGAGGAGCCTTTCCTTATTGGCCCAGGCCGTGGATCCCAGACACCCCAATATGATGACAGAT GTGGTTCAGCTTCTCTCTGCGGTATGCATTGTAGGGGAAGAAAGCATCCTTccaccggt	
mDia2-K12E	ctcgagATGAGTGAGGAGAGGAGCCTTTCCTTATTGGCCgAAGCCGTGGATCCCAGACACCCCAATATGATGACAGAT GTGGTTAAACTTCTCTCTGCGGTATGCATTGTAGGGGAAGAAAGCATCCTTccaccggt	
mDia2-K27E	ctcgagATGAGTGAGGAGAGGAGCCTTTCCTTATTGGCCAAAGCCGTGGATCCCAGACACCCCAATATGATGACAGAT GTGGTTgAACTTCTCTCTGCGGTATGCATTGTAGGGGAAGAAAGCATCCTTccaccggt	
mDia2-K12E-K27E	ctcgagATGAGTGAGGAGAGGAGCCTTTCCTTATTGGCCgAAGCCGTGGATCCCAGACACCCCAATATGATGACAGATG TGGTTgAACTTCTCTCTGCGGTATGCATTGTAGGGGAAGAAAGCATCCTTccaccggt	

PrimeScipt RT Reagent Kit with genomic DNA Eraser (Cat. No. RR047A, Takara). qRT–PCR was performed on a CFX 96 Real-Time System (Bio-Rad Laboratories, CA) using the SYBR Premix Ex Taq II Kit (Cat. No. RR820A, Takara). The primers used are shown in Table 3. The expression levels of the target genes were calculated using the ΔΔCT method. GAPDH was used as an internal control.

Cell migration and invasion assays

Wound-healing and transwell migration and invasion assays were performed to assess cell metastatic ability, respectively. The wound-healing assay was performed following the routine workflow (Vang Mouritzen & Jenssen, 2018). The proliferation inhibitor mitomycin C (0.5 μM) was used for pre-treatment (2 h), which sufficiently suppressed HCC cell proliferation without causing significant cytotoxicity. Wound closure was observed and photographed under a microscope 48 h after scratching. Migration distance was then measured. For the transwell assay, HCC cells were loaded in the upper chamber (for invasion assay, the upper chamber was precoated with 10 mg/ml growth factor-reduced Matrigel). Complete medium containing 20% fetal bovine serum was added to the bottom wells of the transwell chambers (Cat. No. CLS3470-48EA, Corning Inc., Cambridge, MA) covered Matrigel (Cat. No. 356235, Corning Inc., Cambridge, MA). After incubation for 24 h (48 h for the invasion assay), cells that migrated onto the lower surface of the filter were fixed, stained with crystal violet, and photographed. Migration and invasion were determined by counting cells in five microscopic fields per well, and the extent of migration and invasion were expressed as the average number of cells per microscopic field.

Fluorescence imaging

For *in vivo* tracking, different groups of HCC cells were infected with firefly luciferase-expressing lentivirus (Genepharma, Shanghai, China). HCC formation and metastases were imaged using bioluminescence. D-luciferin (Xenogen, Hopkinton, MA) at 100 mg/kg was injected intraperitoneally into mice, and bioluminescence was detected using an IVIS 100 Imaging System (Xenogen). The resulting grayscale photographic and pseudo-colored luminescent images were automatically superimposed using the IVIS Living Image (Xenogen) software.

To visualize F-actin, the HCC cells and tissues were fixed for 30 min at RT in 4% paraformaldehyde in PBS and stained with Actin-stain™ 555 Fluorescent Phalloidin in 0.1% Triton-X 100 (Cat. No. 9002-93-1, MP Biomedicals, CA) according to the supplier's instructions. LifeAct-mCherry transduction was also performed using a customized retrovirus (Genepharma, Shanghai, China) according to the supplier's instructions, by addition of HiTransG (GeneChem, Shanghai, China), a viral transduction reagent, to achieve a MOI of 200 IU/cell. Immunofluorescence was performed as described previously (Ji *et al*, 2021). Then, the HCC cells and tissues were viewed using an Olympus FV3000 laser-scanning confocal microscope (Tokyo, Japan). HCC cells were imaged using a 100× oil immersion objective (OLYMPUS UPLAPO 100XOHR, numerical aperture (NA): 1.50, working distance (WD): 0.12 mm) with the dwell time of 2 μs and the scan size of 1,024 × 1,024. Pinhole size is 319 μm. HCC tissue samples were imaged using a 60× oil immersion objective (OLYMPUS UPLSAPO60XO, NA: 1.42, WD: 0.15 mm) with the dwell time of 2 μs and the scan size of 1,024 × 1,024. The pinhole size is 202 μm. For the blue channel, samples were excited with a 405 nm laser (Coherent OBIS, maximum power: 50 mW, nominal power: 14.8 mW at the fiber end where laser enters to confocal unit, laser intensity: 3.7%). Photomultiplier tubes (PMT, Hamamatsu Photonics) were used to convert light into electrical signals. PMT Voltage: 667V. Detection wavelength: 430–470 nm. Gain: 1.0×, Offset: 0%. For the green channel, samples were excited with a 488 nm laser (Coherent OBIS, maximum power: 20 mW, nominal power: 11.6 mW, laser intensity: 3.2%). PMT Voltage: 676V. Detection wavelength: 500–540 nm. Gain: 1.0×, Offset: 0%. For the red channel, samples were excited with a 561 nm laser (Coherent OBIS, maximum power: 20 mW, nominal power: 12.3 mW, laser intensity: 3.1%). PMT Voltage: 641V. Detection wavelength: 570–670 nm. Gain: 1.0×, Offset: 0%.

The fluorescence intensity in the region of nucleus was measured by ImageJ software (National Institutes of Health, MD), and the values of the knockout or overexpression groups were divided by the mean values of the control group to obtain the fluorescence intensity of the relative nuclear actin. For imaging of nuclear F-actin filaments, HCC cells stained with Phalloidin (or transfected with the LifeAct-mCherry) was imaged with 10–15 Z-stacks at 0.8 μm distance (20–25 Z-stacks for HCC tissues). 3D volume reconstructions were done in Imaris software (Bitplane AG, Zurich, Switzerland).

ATAC-seq and RNA-seq

Library construction and sequencing were performed by LC Biotech (Hangzhou, China) on an Illumina Novaseq 6000 platform. ATAC-seq was performed on 5×10^4 HCC cells following the original protocol (Buenrostro *et al*, 2013) and 150 bp paired-end sequencing was performed, yielding an average of 120 M reads/sample. The clean reads were mapped to the human genome (assembly GRCh38) using Bowtie2 v2.3.4.1. Peak detection was performed using the MACS v2.1.2 peak finding algorithm with 0.05, set as the *q*-value cutoff (Zhang *et al*, 2008). Differential peaks were identified using the DiffBind algorithms with q-values of 0.05, in the two comparison groups. For RNA-seq, total RNA was isolated and purified using TRIzol reagent (Cat. No. 9109, Takara), followed by RNA library preparation using the Illumina TruSeq Stranded mRNA Library Prep kit (Cat. No. RS-122-2103, Illumina, CA). All RNA-seq libraries were sequenced with a read length of paired-end 150 bp, and a final of over 50 million reads per sample. Reads were aligned and gene counts were determined using STAR. EdgeR was used for batch correction, normalization, and differential gene expression analysis. Gene set enrichment analysis (GSEA)7 was performed according to recommended parameters.

Gelatin Zymography

Conditioned cell supernatants were electrophoresed under non-reducing conditions (Laemmli) into gelatin gels (1 mg/ml). After electrophoresis, gels were washed with the eluent (Tris–HCl 50 mM, $CaCl_2$ 5 mM, $ZnCl_2$ 1 μM, 2.5% Triton X-100) for 1 h (change the eluent every 15 min) and rinsed twice with the Buffer PW (Tris–HCl 50 mM, $CaCl_2$ 5 mM, and $ZnCl_2$ 1 μM) for 5 min and then incubated for 42 h with the incubation buffer (Tris–HCl 50 mM, NaCl 0.2 M, $CaCl_2$ 5 mM, $ZnCl_2$ 1 μM, 0.02% Brij-35). Gels were stained with 0.25% Coomassie Blue in 30% methanol and 10% acetic acid for 3 h and then destained in 20% methanol and 10% acetic acid until the MMPs were detected as clear bands against a blue background (liquid was changed every 30 min).

Endothelial cell tube formation assay

To verify the effect of treatment cells on angiogenesis, Matrigel (Cat. No. 356235, Corning Inc., Cambridge, MA) was coated in 96-well plates at 37°C for 0.5 h. Then, 3×10^4 HUVECs were seeded and co-cultured with the culture supernatant of the treatment cell at 37°C for 4–6 h. After incubation, the formation of endothelial tubules was observed and photographed under light microscope.

Metabolomics analysis

Targeted metabolomics was conducted by Shanghai Bioprofile Technology Co. Ltd (Shanghai, China) to quantitatively measure the metabolites associated with glycolysis and TCA in the mitochondrial and cytosolic fractions. The mitochondrial isolation kit (Cat. No. C3601, Beyotime, Shanghai, China), which enriched the mitochondrial fraction from the cytosolic fraction of mammalian cells, was used in the present study. Briefly, HCC cells were homogenized with a mitochondrial separation reagent and centrifuged at 1,000 *g* to remove the nucleus and plasma membrane fragments. The supernatant was transferred and centrifuged at 11,000 *g*, and the supernatant was collected as the cytosolic fraction, while the Pellet is intact mitochondria. The mitochondrial protein COX4 and cytoplasmic tubulin were used as markers to identify the purity of each fraction.

The metabolites were then extracted from the cell residue with 1 ml of precooled methanol/acetonitrile/water (v/v/v, 2:2:1) under sonication for 1 h in ice baths. The mixture was incubated at −20°C for at least 1 h, followed by centrifugation at 14,000 *g* at 4°C for 20 min, and the solvent was evaporated using nitrogen. The metabolites were re-dissolved in 50% methanol and then transferred to a sampling vial for LC-MS analysis. LC-MS analysis was performed using a Shimadzu Nexera LC-30AD UHPLC system (Shimadzu, Japan) coupled to an AB SCIEX QTRAP 5500 mass spectrometer (AB Sciex, Framingham, MA). To ensure data quality for metabolic profiling, quality control (QC) samples were prepared by pooling aliquots of all samples that were representative of all samples under analysis and were used for data normalization. QC samples were prepared and analyzed using the same procedure as that used for the experimental samples in each batch.

Metabolites were detected in electrospray negative-ionization and positive-ionization modes. The 2 μl samples were injected sequentially with an LC autosampler. Raw MRM data files were processed by peak finding, alignment, extraction, and filtering using the MultiQuant software. Serial dilutions of each standard metabolite were prepared for LC-MS analysis. The peak area of each standard metabolite from the serially diluted reference standard solution was used to construct a calibration curve. A calibration curve with a correlation coefficient (R^2) higher than 0.99 was acceptable. The quantitative concentrations of metabolites were calculated based on a calibration curve.

Acetyl-CoA, malonyl-CoA, and lactate measurement

For the measurement of acetyl-CoA, HCC cells were harvested in RIPA buffer, sonicated, and precipitated with 1.0 M Perchloric Acid (PCA, Cat. No.30755, Sigma, CA). After centrifugation, the supernatant was recovered and neutralized by the addition of potassium bicarbonate, and the precipitates were removed by centrifugation. The acetyl-CoA concentration in the supernatant was determined in triplicate using an acetyl-CoA assay kit (Cat. No. MAK039, Sigma, CA) according to the manufacturer's instructions. For the measurement of malonyl-CoA, HCC cells were sonicated and centrifuged. The supernatant was used to determine malonyl-CoA concentration in triplicate using a human malonyl coenzyme A ELISA kit (Cat. No. CSB-E13877h, Cusabio Biotech Co., Ltd. Wuhan, China), according to the manufacturer's instructions. For the measurement of lactate levels, HCC cells were sonicated and centrifuged. The supernatant was used to determine lactate concentration in triplicate using the Lactate Colorimetric Assay Kit (Cat. No. K627-100, BioVision, Milpitas) according to the manufacturer's instructions.

Assessment of extracellular acidification rate (ECAR)

The ECAR was assessed using an Agilent Seahorse XFe96 Analyzer. Briefly, HCC cells were plated in a 96-well Seahorse assay plate (Agilent) at a density of 5×10^4 cells/well and allowed to adhere for 1 h in an incubator lacking CO_2. ECAR was measured at baseline and following sequential injections of glucose (10 mM), oligomycin (1.0 μM), and 2-DG (50 nM), according to the XF glycolysis stress test protocol. Therefore, glycolysis was calculated as maximum rate measurement before Oligomycin injection minus last rate measurement before glucose injection. While glycolytic capacity was calculated as maximum rate measurement after Oligomycin injection minus last rate measurement before glucose injection.

Acetyl-CoA carboxylase (ACC) activity measurement

The ACC assay kit (Cat. No. BC0410, Solarbio, Beijing, China) was used to measure the activity of ACC according to the manufacturer's instructions. The determination of the ACC was based on the reaction of acetyl-CoA being catalyzed to inorganic phosphorus and malonyl-CoA. The inorganic phosphorus was further determined by a reaction with molybdenum blue, and the absorbance was read at 660 nm. Standard curve was constructed using known amounts of phosphate in combination with the molybdenum blue reagent.

Quantification of neutral lipid

The lipophilic fluorescence dye BODIPY 493/503 (Cat. No. D3922, Thermo Fisher, Waltham) was used to monitor the content of neutral lipids in HCC cells according to the manufacturer's instructions. Briefly, HCC cells were fixed with 4% paraformaldehyde and stained with BODIPY 493/503 at a concentration of 1 μg/ml at 37°C for 45 min, and then, nuclei were counterstained by Hoechst (10 μg/ml) for 15 min. Images were obtained using Olympus FV3000 laser-scanning confocal microscope (Tokyo, Japan).

Statistical analysis

GraphPad Prism 8.3.1 (GraphPad Software Inc.) was used to analyze the data. The data were presented as mean ± SEM. Values of $P < 0.05$ were considered statistically significant. Correlation between continuous variables was assessed using the Pearson correlation coefficient for normally distributed variables. Two-tailed Student's *t*-test was performed to examine differences between two

groups. Kaplan–Meier survival curve was plotted and compared by log-rank test.

Data availability

All data needed to evaluate the conclusions in the paper are present in the paper and/or the Supplementary Materials. The metabolomic raw data were deposited in MetaboLights (www.ebi.ac.uk/metabolights/MTBLS4307).

Expanded View for this article is available online.

Acknowledgements
The authors thank Professor Yongzhan Nie (Xijing Hospital of Digestive Diseases, FMMU) for donating the experimental mice, and Professor Xin Chen (University of California) for donating the vectors used in the hydrodynamic injection. The authors also thank Jingjie PTM BioLab (Hangzhou) Co. Inc. for illustrative drawings and also Dr. Yuansheng Liu from Olympus for his technical support. This work was supported by the National Natural Science Foundation of China (81772935, 82072722, 81830070, and 81672340) and the State Key Laboratory of Cancer Biology Project (CBSKL2019ZZ26).

Author contributions
Qichao Huang: Data curation; Formal analysis; Supervision; Writing—original draft; Project administration; Writing—review & editing. **Dan Wu:** Software; Validation; Investigation; Methodology. **Jing Zhao:** Data curation; Validation; Investigation; Methodology; Writing—review & editing. **Zeyu Yan:** Validation; Methodology. **Lin Chen:** Data curation; Investigation; Methodology. **Shanshan Guo:** Data curation; Project administration. **Dalin Wang:** Data curation; Software; Methodology. **Chong Yuan:** Data curation; Validation; Methodology. **Yinping Wang:** Validation; Methodology. **Xiaoli Liu:** Software; Validation. **Jinliang Xing:** Conceptualization; Resources; Software; Supervision; Validation; Methodology; Project administration; Writing—review & editing.

In addition to the CRediT author contributions listed above, the contributions in detail are:

QH designed the overall study, analyzed the results, and wrote the manuscript; DWu and JZ performed most experiments, analyzed data, and wrote the part of manuscript; ZY participated in the *in vivo* study, analyzed data, and wrote the part of manuscript; LC participated in the part of animal study; SG participated in the analysis of ATCA and transcriptome data. DWa, XZ and CY participated *in vitro* study; YW and XL participated in Immunohistochemistry and western blot; JX supervised the work, provided administrative support, and revised the paper.

Disclosure and competing interests statement
The authors declare that they have no conflict of interest.

References

An S, Yoon J, Kim H, Song J-J, Cho U-S (2017) Structure-based nuclear import mechanism of histones H3 and H4 mediated by Kap123. *Elife* 6: e30244

Araujo LF, Siena ADD, Plaça JR, Brotto DB, Barros II, Muys BR, Biagi CAO, Peronni KC, Sousa JF, Molfetta GA *et al* (2018) Mitochondrial transcription factor A (TFAM) shapes metabolic and invasion gene signatures in melanoma. *Sci Rep* 8: 14190

Baarlink C, Plessner M, Sherrard A, Morita K, Misu S, Virant D, Kleinschnitz E-M, Harniman R, Alibhai D, Baumeister S *et al* (2017) A transient pool of nuclear F-actin at mitotic exit controls chromatin organization. *Nat Cell Biol* 19: 1389 – 1399

Baarlink C, Wang H, Grosse R (2013) Nuclear actin network assembly by formins regulates the SRF coactivator MAL. *Science* 340: 864 – 867

Buenrostro JD, Giresi PG, Zaba LC, Chang HY, Greenleaf WJ (2013) Transposition of native chromatin for fast and sensitive epigenomic profiling of open chromatin, DNA-binding proteins and nucleosome position. *Nat Methods* 10: 1213 – 1218

Caridi CP, D'Agostino C, Ryu T, Zapotoczny G, Delabaere L, Li X, Khodaverdian VY, Amaral N, Lin E, Rau AR *et al* (2018) Nuclear F-actin and myosins drive relocalization of heterochromatic breaks. *Nature* 559: 54 – 60

Chandrasekaran K, Muragundla A, Demarest TG, Choi J, Sagi AR, Najimi N, Kumar P, Singh A, Ho C-Y, Fiskum G *et al* (2017) mGluR2/3 activation of the SIRT1 axis preserves mitochondrial function in diabetic neuropathy. *Ann Clin Transl Neurol* 4: 844 – 858

Chen X, Calvisi DF (2014) Hydrodynamic transfection for generation of novel mouse models for liver cancer research. *Am J Pathol* 184: 912 – 923

Figlia G, Willnow P, Teleman AA (2020) Metabolites regulate cell signaling and growth via covalent modification of proteins. *Dev Cell* 54: 156 – 170

Fu Z, Ye J, Dean JW, Bostick JW, Weinberg SE, Xiong L, Oliff KN, Chen ZE, Avram D, Chandel NS *et al* (2019) Requirement of mitochondrial transcription factor A in tissue-resident regulatory T cell maintenance and function. *Cell Rep* 28: 159 – 171.e154

Galván-Peña S, Carroll RG, Newman C, Hinchy EC, Palsson-McDermott E, Robinson EK, Covarrubias S, Nadin A, James AM, Haneklaus M *et al* (2019) Malonylation of GAPDH is an inflammatory signal in macrophages. *Nat Commun* 10: 338

Gao P, Zhang H, Dinavahi R, Li F, Xiang Y, Raman V, Bhujwalla ZM, Felsher DW, Cheng L, Pevsner J *et al* (2007) HIF-dependent antitumorigenic effect of antioxidants *in vivo*. *Cancer Cell* 12: 230 – 238

Huang Q, Li J, Xing J, Li W, Li H, Ke X, Zhang J, Ren T, Shang Y, Yang H *et al* (2014) CD147 promotes reprogramming of glucose metabolism and cell proliferation in HCC cells by inhibiting the p53-dependent signaling pathway. *J Hepatol* 61: 859 – 866

Huang Q, Zhan L, Cao H, Li J, Lyu Y, Guo XU, Zhang J, Ji L, Ren T, An J *et al* (2016) Increased mitochondrial fission promotes autophagy and hepatocellular carcinoma cell survival through the ROS-modulated coordinated regulation of the NFKB and TP53 pathways. *Autophagy* 12: 999 – 1014

Huang R, Rofstad EK (2018) Integrins as therapeutic targets in the organ-specific metastasis of human malignant melanoma. *J Exp Clin Cancer Res* 37: 92

Ji L, Zhao Y, He L, Zhao J, Gao T, Liu F, Qi B, Kang F, Wang G, Zhao Y *et al* (2021) AKAP1 deficiency attenuates diet-induced obesity and insulin resistance by promoting fatty acid oxidation and thermogenesis in brown adipocytes. *Adv Sci* 8: 2002794

Koh J-H, Johnson ML, Dasari S, LeBrasseur NK, Vuckovic I, Henderson GC, Cooper SA, Manjunatha S, Ruegsegger GN, Shulman GI *et al* (2019) TFAM enhances fat oxidation and attenuates high-fat diet-induced insulin resistance in skeletal muscle. *Diabetes* 68: 1552 – 1564

Kristó I, Bajusz I, Bajusz C, Borkúti P, Vilmos P (2016) Actin, actin-binding proteins, and actin-related proteins in the nucleus. *Histochem Cell Biol* 145: 373 – 388

Lan L, Guo M, Ai Y, Chen F, Zhang YA, Xia L, Huang D, Niu L, Zheng Y, Suzuki C *et al* (2017) Tetramethylpyrazine blocks TFAM degradation and up-

regulates mitochondrial DNA copy number by interacting with TFAM. *Biosci Rep* 37: BSR20170319

Li T, Diner BA, Chen J, Cristea IM (2012) Acetylation modulates cellular distribution and DNA sensing ability of interferon-inducible protein IFI16. *Proc Natl Acad Sci USA* 109: 10558 – 10563

Liu X, Zhang Y, Ni M, Cao H, Signer RAJ, Li D, Li M, Gu Z, Hu Z, Dickerson KE *et al* (2017) Regulation of mitochondrial biogenesis in erythropoiesis by mTORC1-mediated protein translation. *Nat Cell Biol* 19: 626 – 638

Llovet JM, Kelley RK, Villanueva A, Singal AG, Pikarsky E, Roayaie S, Lencioni R, Koike K, Zucman-Rossi J, Finn RS (2021) Hepatocellular carcinoma. *Nat Rev Dis Primers* 7: 6

Lu M, Zhu W-W, Wang X, Tang J-J, Zhang K-L, Yu G-Y, Shao W-Q, Lin Z-F, Wang S-H, Lu LU *et al* (2019) ACOT12-dependent alteration of acetyl-CoA drives hepatocellular carcinoma metastasis by epigenetic induction of epithelial-mesenchymal transition. *Cell Metab* 29: 886 – 900.e885

Lutz-Bonengel S, Niederstätter H, Naue J, Koziel R, Yang F, Sänger T, Huber G, Berger C, Pflugradt R, Strobl C *et al* (2021) Evidence for multi-copy Mega-NUMTs in the human genome. *Nucleic Acids Res* 49: 1517 – 1531

Martin DB, Vagelos PR (1962) The mechanism of tricarboxylic acid cycle regulation of fatty acid synthesis. *J Biol Chem* 237: 1787 – 1792

Martínez-Reyes I, Chandel NS (2020) Mitochondrial TCA cycle metabolites control physiology and disease. *Nat Commun* 11: 102

Miki T, Okawa K, Sekimoto T, Yoneda Y, Watanabe S, Ishizaki T, Narumiya S (2009) mDia2 shuttles between the nucleus and the cytoplasm through the importin-{alpha}/{beta}- and CRM1-mediated nuclear transport mechanism. *J Biol Chem* 284: 5753 – 5762

Nardozzi JD, Lott K, Cingolani G (2010) Phosphorylation meets nuclear import: a review. *Cell Commun Signal* 8: 32

Peng C, Lu Z, Xie Z, Cheng Z, Chen Y, Tan M, Luo H, Zhang YI, He W, Yang KE *et al* (2011) The first identification of lysine malonylation substrates and its regulatory enzyme. *Mol Cell Proteomics* 10: M111.012658

Percipalle P, Vartiainen M (2019) Cytoskeletal proteins in the cell nucleus: a special nuclear actin perspective. *Mol Biol Cell* 30: 1781 – 1785

Plessner M, Melak M, Chinchilla P, Baarlink C, Grosse R (2015) Nuclear F-actin formation and reorganization upon cell spreading. *J Biol Chem* 290: 11209 – 11216

Qiao Y, Xu M, Tao J, Che L, Cigliano A, Monga SP, Calvisi DF, Chen X (2018) Oncogenic potential of N-terminal deletion and S45Y mutant β-catenin in promoting hepatocellular carcinoma development in mice. *BMC Cancer* 18: 1093

Roessler S, Lin G, Forgues M, Budhu A, Hoover S, Simpson RM, Wu X, He P, Qin L-X, Tang Z-Y *et al* (2015) Integrative genomic and transcriptomic characterization of matched primary and metastatic liver and colorectal carcinoma. *Int J Biol Sci* 11: 88 – 98

Schrank BR, Aparicio T, Li Y, Chang W, Chait BT, Gundersen GG, Gottesman ME, Gautier J (2018) Nuclear ARP2/3 drives DNA break clustering for homology-directed repair. *Nature* 559: 61 – 66

Spichal M, Brion A, Herbert S, Cournac A, Marbouty M, Zimmer C, Koszul R, Fabre E (2016) Evidence for a dual role of actin in regulating chromosome organization and dynamics in yeast. *J Cell Sci* 129: 681 – 692

Sugden B, Warren N (1989) A promoter of Epstein-Barr virus that can function during latent infection can be transactivated by EBNA-1, a viral protein required for viral DNA replication during latent infection. *J Virol* 63: 2644 – 2649

Toki N, Kagami S, Kurita T, Kawagoe T, Matsuura Y, Hachisuga T, Matsuyama A, Hashimoto H, Izumi H, Kohno K (2010) Expression of mitochondrial transcription factor A in endometrial carcinomas: clinicopathologic correlations and prognostic significance. *Virchows Arch* 456: 387 – 393

Ulferts S, Prajapati B, Grosse R, Vartiainen MK (2021) Emerging properties and functions of actin and actin filaments inside the nucleus. *Cold Spring Harb Perspect Biol* 13: a040121

Vang Mouritzen M, Jenssen H (2018) Optimized scratch assay for *in vitro* testing of cell migration with an automated optical camera. *J Vis Exp* 138: 57691 .

Venit T, Mahmood SR, Endara-Coll M, Percipalle P (2020) Nuclear actin and myosin in chromatin regulation and maintenance of genome integrity. *Int Rev Cell Mol Biol* 355: 67 – 108

Wang C, Cigliano A, Jiang L, Li X, Fan B, Pilo MG, Liu Y, Gui B, Sini M, Smith JW *et al* (2015) 4EBP1/eIF4E and p70S6K/RPS6 axes play critical and distinct roles in hepatocarcinogenesis driven by AKT and N-Ras proto-oncogenes in mice. *Hepatology* 61: 200 – 213

Wen Y-A, Xiong X, Scott T, Li AT, Wang C, Weiss HL, Tan LI, Bradford E, Fan TWM, Chandel NS *et al* (2019) The mitochondrial retrograde signaling regulates Wnt signaling to promote tumorigenesis in colon cancer. *Cell Death Differ* 26: 1955 – 1969

Woo DK, Green PD, Santos JH, D'Souza AD, Walther Z, Martin WD, Christian BE, Chandel NS, Shadel GS (2012) Mitochondrial genome instability and ROS enhance intestinal tumorigenesis in APC(Min/+) mice. *Am J Pathol* 180: 24 – 31

Wu B, Qiu J, Zhao TV, Wang Y, Maeda T, Goronzy IN, Akiyama M, Ohtsuki S, Jin KE, Tian LU *et al* (2020) Succinyl-CoA ligase deficiency in pro-inflammatory and tissue-invasive T cells. *Cell Metab* 32: 967 – 980.e965

Xu X, Liu Z, Zhou L, Xie H, Cheng J, Ling Q, Wang J, Guo H, Wei X, Zheng S (2015) Characterization of genome-wide TFCP2 targets in hepatocellular carcinoma: implication of targets FN1 and TJP1 in metastasis. *J Exp Clin Cancer Res* 34: 6

Yang S, He X, Zhao J, Wang D, Guo S, Gao T, Wang G, Jin C, Yan Z, Wang N *et al* (2021) Mitochondrial transcription factor A plays opposite roles in the initiation and progression of colitis-associated cancer. *Cancer Commun* 41: 695 – 714

Ye Q-H, Qin L-X, Forgues M, He P, Kim JW, Peng AC, Simon R, Li Y, Robles AI, Chen Y *et al* (2003) Predicting hepatitis B virus-positive metastatic hepatocellular carcinomas using gene expression profiling and supervised machine learning. *Nat Med* 9: 416 – 423

Yoshida Y, Hasegawa J, Nezu R, Kim YK, Hirota M, Kawano K, Izumi H, Kohno K (2011) Clinical usefulness of mitochondrial transcription factor A expression as a predictive marker in colorectal cancer patients treated with FOLFOX. *Cancer Sci* 102: 578 – 582

Zhang Y, Liu T, Meyer CA, Eeckhoute J, Johnson DS, Bernstein BE, Nusbaum C, Myers RM, Brown M, Li W *et al* (2008) Model-based analysis of ChIP-Seq (MACS). *Genome Biol* 9: R137

Zhou G, Dada LA, Wu M, Kelly A, Trejo H, Zhou Q, Varga J, Sznajder JI (2009) Hypoxia-induced alveolar epithelial-mesenchymal transition requires mitochondrial ROS and hypoxia-inducible factor 1. *Am J Physiol Lung Cell Mol Physiol* 297: L1120 – 1130

Zuo Y, Qu C, Tian Y, Wen Y, Xia S, Ma M (2021) The HIF-1/SNHG1/miR-199a-3p/TFAM axis explains tumor angiogenesis and metastasis under hypoxic conditions in breast cancer. *BioFactors* 47: 444 – 460

